

# Does the HCN/CO ratio trace the fraction of gravitationally-bound gas?

## II. Variations in CO and HCN Emissivity

Ashley R. Bemis<sup>1,2,3</sup>, Christine D. Wilson<sup>4</sup>, Piyush Sharda<sup>1</sup>, Ian D. Roberts<sup>2,3,1</sup>, and Hao He<sup>5</sup>

<sup>1</sup> Leiden Observatory, Leiden University, PO Box 9513, 2300 RA Leiden, The Netherlands

<sup>2</sup> Department of Physics & Astronomy, University of Waterloo, Waterloo, ON N2L 3G1, Canada

<sup>3</sup> Waterloo Centre for Astrophysics, University of Waterloo, 200 University Ave W, Waterloo, ON N2L 3G1, Canada, Canada

<sup>4</sup> Department of Physics & Astronomy, McMaster University, 1280 Main St W, Hamilton ON L8S 4M1, Canada

<sup>5</sup> Argelander-Institut für Astronomie, Universität Bonn, Auf dem Hügel 71, 53121 Bonn, Germany

October 2, 2024

### ABSTRACT

Using the non-LTE radiative transfer code RADEX, we model emissivities of the HCN and CO  $J = 1 - 0$  transitions across a grid of molecular cloud models encapsulating observed properties spanning from normal star forming galaxies to more extreme merging systems. These models are compared with archival observations of the HCN and CO  $J = 1 - 0$  transitions, in addition to the radio continuum at 93 GHz for 10 nearby galaxies. We combine these model emissivities with predictions of gravoturbulent models of star formation presented in the first paper in this series. In particular, we explore the impact of excitation and optical depth on CO and HCN emission and assess if the HCN/CO ratio tracks the fraction of gravitationally-bound dense gas,  $f_{\text{grav}}$ , in molecular clouds. We find that our modelled HCN/CO ratios are consistent with the measurements within our sample, and our modelled HCN and CO emissivities are consistent with the results of observational studies of nearby galaxies and clouds in the Milky Way. CO emission shows a wide range of optical depths across different environments, ranging from optically thick in normal galaxies to moderately optically thin in more extreme systems. HCN appears only moderately optically thick and shows significant subthermal excitation in both normal and extreme galaxies. We find an anticorrelation between HCN/CO and  $f_{\text{grav}}$ , which implies that the HCN/CO ratio is not a reliable tracer of  $f_{\text{grav}}$ . Instead this ratio appears to best track gas at moderate densities ( $n > 10^{3.5} \text{ cm}^{-3}$ ), which is below the typically assumed dense gas threshold of  $n > 10^{4.5} \text{ cm}^{-3}$ . We also find that variations in CO emissivity depend strongly on optical depth, which is a product of variations in the dynamics of the cloud gas. HCN emissivity is more strongly dependent on excitation, as opposed to optical depth, and thus does not necessarily track variations in CO emissivity. We further conclude that a single line ratio, such as HCN/CO, will not consistently track the fraction of gravitationally-bound, star-forming gas if the critical density for star formation varies in molecular clouds. This work highlights important uncertainties that need to be considered when observationally applying an HCN conversion factor in order to estimate the dense (i.e.  $n > 10^{4.5} \text{ cm}^{-3}$ ) gas content in nearby galaxies.

### 1. Introduction

The HCN/CO ratio is commonly used to assess the fraction of dense gas ( $\gtrsim 10^4 - 10^5 \text{ cm}^{-3}$ ) that might be associated with star formation in external galaxies. The seminal work by Gao & Solomon (2004a,b) found a linear scaling (slope of unity) between the logarithm of the HCN luminosity and the star formation rate as traced in the infrared (IR)<sup>1</sup> for a diverse sample of galaxies, including normal disk galaxies as well as more extreme Ultra-Luminous and Luminous Infrared Galaxies (U/LIRGs). This correlation suggests that HCN is a useful tracer of star-forming gas for a range of galaxy types. The linear scaling between  $L_{\text{IR}}$  and  $L_{\text{HCN}}$  also implies that the critical density for HCN  $J = 1 - 0$  emission,  $n_{\text{crit,HCN}}$ , is close to a common, mean threshold density,  $n_{\text{thresh}}$ , that is important for star formation. Although individual galaxies have scatter in the  $L_{\text{IR}}$  and  $L_{\text{HCN}}$  relationship, a linear scaling implies that the average  $L_{\text{IR}}/L_{\text{HCN}} = 900 L_{\odot} (\text{K km s}^{-1} \text{ pc}^2)$  (Gao & Solomon 2004b) ratio is relatively constant over many orders of magnitude. However, systematic deviations from linearity have since been found in U/LIRGs (Graciá-Carpio et al. 2008; García-Burillo et al. 2012),

at sub-kpc scales in disk galaxies (Usero et al. 2015; Chen et al. 2015; Gallagher et al. 2018b; Querejeta et al. 2019; Jiménez-Donaire et al. 2019; Bešlić et al. 2021; Neumann et al. 2023), and at sub-kpc scales in galaxy mergers (Bigiel et al. 2015; Bemis & Wilson 2019). These non-linearities do not appear associated with the presence of an active galactic nucleus (AGN), which otherwise could enhance HCN emissivity via infrared pumping (Sakamoto et al. 2010). In the absence of an AGN, these variations in emissivity can be interpreted as a fundamental difference in the depletion time of dense gas within different systems, which may signal a connection between star formation and environment within galaxies.

Variations are also seen in the star formation efficiency of dense gas in our own Milky Way. Gas in the Central Molecular Zone (CMZ) of the Milky Way is dense ( $n \sim 10^4 \text{ cm}^{-3}$ ) and warm ( $T \sim 65 \text{ K}$ ) compared to gas in the disk ( $n_0 \sim 10^2 \text{ cm}^{-3}$ ,  $T \sim 10 \text{ K}$ , Rathborne et al. 2014; Ginsburg et al. 2016). Despite their abundance of dense gas (Mills 2017), some clouds in the CMZ display a lack of star formation (Longmore et al. 2013; Kruijssen et al. 2014; Walker et al. 2018). CMZ clouds are experiencing high external pressures ( $\sim 10^8 \text{ K cm}^{-3}$ ), and it is theorized that their lack of star forming activity may be due to a higher star formation threshold density as a result of higher

<sup>1</sup> We note that a slope of unity between  $\log L_{\text{IR}}$  and  $\log L_{\text{HCN}}$  also implies a linear scaling between  $L_{\text{IR}}$  and  $L_{\text{HCN}}$ .

internal turbulent pressures (Walker et al. 2018). Additionally, shear from solenoidal turbulence may also suppress the onset of star formation in the CMZ (Federrath et al. 2016a). A lack of star formation in dense gas traced by HCN is also apparent in the centers of nearby disk galaxies (Gallagher et al. 2018b; Querejeta et al. 2019; Jiménez-Donaire et al. 2019; Bešlić et al. 2021; Neumann et al. 2023) and the nuclei of the Antennae galaxies (NGC4038/9, Bemis & Wilson 2019). Gas density is well-constrained in the CMZ, suggesting that there are true variations in star formation from dense gas in this environment relative to the Milky Way disk. Many studies of external galaxies rely on a single molecular gas tracer, HCN, to estimate the dense gas fraction and recent work calls in to question its ability to consistently trace dense gas in molecular clouds (e.g., Kauffmann et al. 2017; Pety et al. 2017; Shimajiri et al. 2017; Barnes et al. 2020; Tafalla et al. 2021, 2023; Santa-Maria et al. 2023, Ngoc Le et al. in prep.). Furthermore, if the star formation threshold density also varies with environment within galaxies, a gas fraction estimate from a single line ratio may not reliably track the fraction of gas above this threshold (Bemis & Wilson 2023; Neumann et al. 2023).

In Bemis & Wilson (2023, hereafter Paper I), we assess the ability of the relative intensity of HCN to CO,  $I_{\text{HCN}}/I_{\text{CO}}$ , to determine the fraction of gravitationally bound gas by comparing the observed star formation properties and HCN/CO ratios in 10 galaxies to the predictions of analytical models of star formation (Krumholz & McKee 2005; Federrath & Klessen 2012; Hennebelle & Chabrier 2011; Burkhardt 2018). In Paper I, we find that trends observed in our sample in dense gas traced by  $I_{\text{HCN}}$ , SFR traced by the radio continuum at 93 GHz, and total molecular gas traced by  $I_{\text{CO}}$  are best reproduced by gravo-turbulent models of star formation with varying star formation thresholds under the assumption that  $I_{\text{HCN}}/I_{\text{CO}}$  is tracing the fraction of gas above a relatively fixed density, such as  $n_{\text{H}_2} \gtrsim 10^{4.5} \text{ cm}^{-3}$ , but not necessarily the fraction of gas that is gravitationally bound or star-forming. Furthermore, in Paper I we show that turbulent models of star formation with varying star formation thresholds predict an *increase* in the depletion time of dense gas at  $n_{\text{H}_2} \gtrsim 10^{4.5} \text{ cm}^{-3}$  in clouds with higher dense gas fractions due to higher levels of turbulence. This corroborates observations in the CMZ where star formation appears suppressed relative to the amount of dense gas mass, estimates of turbulent pressure ( $P_{\text{turb}}$ ) appear higher, and the dominant mode of turbulence may be more solenoidal compared to spiral arms (Federrath et al. 2016a; Walker et al. 2018). Similar trends are observed in galaxy centers (Gallagher et al. 2018b; Querejeta et al. 2019; Jiménez-Donaire et al. 2019; Bešlić et al. 2021) and in the nuclei of the Antennae (Paper I), although estimates of the dominant turbulent mode are unavailable for these studies.

One key uncertainty in these results is the ratio of the emissivities of HCN and CO, i.e. the conversion of HCN or CO intensity to gas column density, and whether systematic variations in HCN and CO emissivity can occur in such a way that may also contribute to the observed trends. The CO conversion factor,  $\alpha_{\text{CO}}$ , is estimated to vary with excitation (e.g. Narayanan et al. 2012; Narayanan & Krumholz 2014) and metallicity (e.g. Schrubba et al. 2012; Hu et al. 2022a), can be nearly five times lower in U/LIRGs (e.g. Downes et al. 1993), and is lower in the centers of disk galaxies (e.g. Sandstrom et al. 2013). The HCN conversion factor,  $\alpha_{\text{HCN}}$ , is also likely to vary across different systems (Usero et al. 2015), but may not necessarily track  $\alpha_{\text{CO}}$  (Onus et al. 2018). Observations of HCN and  $\text{H}^{13}\text{CN}$  in galaxy centers suggest that HCN is only moderately optically thick (Jiménez-Donaire et al. 2017), unlike CO which typically has

$\tau_{\text{CO}} > 10$ . The original estimate of  $\alpha_{\text{HCN}}$  was made under the assumption of optically-thick emission (Gao & Solomon 2004a,b). Since HCN emission appears only moderately optically thick, variations in the optical depth of HCN emission could impact the accuracy of gas masses using this estimate of the HCN conversion factor. Thus, the HCN/CO intensity ratio may not scale linearly with the fraction of gas  $\gtrsim 10^4 \text{ cm}^{-3}$  due to variations in excitation and optical depth. As we refine our understanding of star formation in galaxies, it is clear we must also adopt a more sophisticated approach to estimating masses using molecular line emission, and we must develop a better understanding of the information that these measurements can provide on star formation.

In this paper, we model emissivities of HCN and CO using the non-LTE radiative transfer code RADEX, (van der Tak et al. 2007; Leroy et al. 2017a) across a grid of cloud models that encapsulates observed trends in cloud properties spanning normal star forming galaxies to U/LIRGs. We assess the impact of variations in optical depth and excitation on the emissivities of HCN and CO across this grid, and we compare our modelling results with the star forming trends observed in the sample of 10 galaxies from Paper I using archival ALMA data of the HCN and CO  $J = 1 \rightarrow 0$  transitions and the radio continuum at 93 GHz (see Wilson et al. 2023 for details on imaging). This sample includes the dense centers of five disk galaxies and five U/LIRGs, (see Table 1 of Paper I). In §2, we describe the model framework that we adopt to derive emissivities using analytical models of star formation (§2.1) as well as the parameter space we consider (§2.3). We present the results of our models and compare these results with observations in §3. Finally, in §4 we provide a brief discussion and summary of our main results. Throughout the text we take ‘‘HCN/CO’’ ratio to mean the ratio between HCN and CO intensities, unless explicitly stated otherwise.

## 2. Model Framework

We model molecular line emissivities using the radiative transfer code RADEX (van der Tak et al. 2007), and we connect these emissivities to gravo-turbulent models of star formation. We present several gravo-turbulent models of star formation in Paper I, which predict clouds have gas density distributions that are either purely lognormal (LN, cf. Padoan & Nordlund 2011; Krumholz & McKee 2005; Federrath & Klessen 2012) or a composite lognormal and power law distribution (LN+PL, cf. Burkhardt et al. 2017). We refer to these distributions as the gas density probability density functions (PDFs) for the remainder of the text. We focus on the results of the composite LN+PL models in this analysis.

### 2.1. Emissivity

We adopt the following definition of the emissivity of a molecular transition (e.g. Leroy et al. 2017a):

$$\epsilon_{\text{mol}} = \frac{I_{\text{mol}}}{N_{\text{H}_2}} = \frac{I_{\text{mol}}}{N_{\text{mol}}/x_{\text{mol}}} \quad (1)$$

where  $I_{\text{mol}}$  is the total line intensity of a molecular transition (in units of  $\text{K km s}^{-1}$ ),  $N_{\text{H}_2}$  is the column density of gas that emits  $I$ ,  $N_{\text{mol}}$  is the molecular column density of an observed molecule (both in units of  $\text{cm}^{-2}$ ), and  $x_{\text{mol}}$  is the fractional abundance of the molecule relative to the molecular hydrogen,  $\text{H}_2$ . The ratio of the HCN and CO emissivities is then given by:

$$\frac{\epsilon_{\text{HCN}}}{\epsilon_{\text{CO}}} = \frac{I_{\text{HCN}}}{I_{\text{CO}}} \frac{N_{\text{CO}}}{N_{\text{HCN}}} \frac{x_{\text{HCN}}}{x_{\text{CO}}} \quad (2)$$

Emissivity is analogous to the inverse of molecular conversion factors ( $\alpha_{\text{mol}} = X_{\text{mol}}/6.3 \times 10^{19}$ , Leroy et al. 2017b), which are commonly used to estimate the mass traced by a molecular transition. In practice, the relationship between the total emissivity of an observed molecular cloud and an appropriate conversion factor also depends on the beam filling fraction and the uniformity of gas properties within the beam (cf. Bolatto et al. 2013).

## 2.2. Cloud Models

Under the assumption that we can derive information of the gas density distribution from estimates of gas velocity dispersion, we build our cloud models using gas density distributions predicted by gravoturbulent models of star formation that employ the *gas density variance – mach number relation* (cf. Eq. 3). There are well-established theories connecting the gas density variance ( $\sigma_{n/n_0}^2$ ) in molecular clouds to mach number (cf. Passot & Vázquez-Semadeni 1998; Beetz et al. 2008; Burkhart et al. 2010; Padoan & Nordlund 2011; Price et al. 2011; Konstandin et al. 2012; Molina et al. 2012; Federrath & Banerjee 2015; Nolan et al. 2015; Pan et al. 2016; Squire & Hopkins 2017; Beattie et al. 2021). In general, these theories predict that the gas density variance increases with mach number, such that (cf. Federrath et al. 2008, 2010; Molina et al. 2012):

$$\sigma_{n/n_0}^2 = b^2 \mathcal{M}^2 \frac{\beta}{\beta + 1} \quad (3)$$

where  $b$  is the turbulent forcing parameter which describes the dominant mode(s) of turbulence (i.e. compressive, mixed, or solenoidal) and spans  $b = 1/3 - 1$  (Federrath et al. 2008, 2010),  $\mathcal{M}$  is the sonic mach number ( $\mathcal{M} = \sqrt{3}\sigma_v/c_s$ , where  $\sigma_v$  is the 1D turbulent velocity dispersion and  $c_s = \sqrt{kT_{\text{kin}}/\mu m_{\text{H}}}$  is the gas sound speed,  $k$  is the Boltzmann constant,  $\mu$  is the mean molecular weight of the gas, and  $m_{\text{H}}$  is the mass of a Hydrogen atom), and  $\beta$  is the ratio of thermal to magnetic pressure (cf. Molina et al. 2012). Numerical work shows that a connection is also expected between the 2D gas density variance,  $\sigma_{\Sigma/\Sigma_0}$ , an observable, and mach number (e.g. Brunt et al. 2010a,b; Burkhart & Lazarian 2012). Thus, resolved studies of the gas column density distribution can, in theory, provide information on the Mach number of the initial turbulent velocity field shaping the dynamics of a cloud. Alternatively, lower-resolution studies that are limited to global cloud measurements (such as is often the case in extragalactic studies) may also be able to derive information on the gas density distribution using estimates of the gas velocity dispersion. We use this as a basis to build our cloud models and our model parameter space, described in detail in section 2.3. We also highlight the relevant uncertainties for this approach, both in this section and in Appendix A.

We note that there are a number of analytical prescriptions describing the gas density distribution (e.g. Krumholz & McKee 2005; Padoan & Nordlund 2011; Hennebelle & Chabrier 2011; Hopkins 2013; Burkhart 2018). For simplicity, we focus on the piecewise lognormal and power law distribution from Burkhart (2018) and note that we do not expect significant changes to our main conclusions if we were to adopt a different prescription. In particular, our models produce gas density distributions with widths and density ranges comparable to those observed in resolved studies of clouds in the Milky Way (cf. Schneider et al. 2022). The piecewise volume density PDF is given in Paper I (Eq. 16) and is originally given in Burkhart (2018) (Eqs. 2 and 6) in terms of the logarithmic density,  $s = \ln(n/n_0)$ , where  $n$  is gas volume density and  $n_0$  is the mean gas volume density. We

refer the reader to Paper I and Burkhart (2018) for a thorough description of these models in terms of the logarithmic density. Here we briefly summarise the main components of these models in terms of the linear gas volume density,  $n$ , which is directly used in our modelling of molecular line emissivities.

Each cloud model is comprised of a piecewise lognormal and power law gas volume density PDF ( $n$  – PDF). The lognormal component of the  $n$  – PDF has a characteristic gas density variance,  $\sigma_{n/n_0}^2$  and mean density,  $n_0$ . We note that the logarithmic gas density PDF (Eq. 16 in Paper I) can be converted to its linear form via  $p_s = n p_n$ . Likewise, the logarithmic variance (Eq. 17 in Paper I),  $\sigma_s^2$ , can be converted to its linear form using  $\sigma_{n/n_0}^2 = \exp(\sigma_s^2) - 1$  (cf. Federrath et al. 2008). The powerlaw component of the  $n$  – PDF is primarily characterized by its slope,  $\alpha_{\text{PL}}$ , and the powerlaw slope of  $p_n$  is related to the slope of  $p_s$  via  $\alpha_{\text{PL}}(n) = \alpha_{\text{PL}}(s) - 1$ . The two components of the  $n$  – PDF are analytically connected such that they are smoothly varying (Burkhart 2018). Similar to Paper I, we fix  $b = 0.4$ , which represents stochastic mixing between the two turbulent forcing modes (Federrath et al. 2010), and we neglect magnetic fields and take  $\beta \rightarrow \infty$ . We illustrate example  $n$  – PDFs in Fig. 1 that are sampled from our model parameter space, described in section 2.3.

## 2.3. The Model Parameter Space

We construct our model parameter space to capture observed trends in cloud properties associated with star-forming molecular gas clouds. As described in section 2.2, each unique model is described by its variance,  $\sigma_n$ , mean density,  $n_0$ , and power law slope,  $\alpha_{\text{PL}}$ . Within  $\sigma_n$  is a dependence on the 1D turbulent gas velocity dispersion,  $\sigma_v$ , and gas kinetic temperature,  $T_{\text{kin}}$ , via the sonic mach number,  $\mathcal{M} = \sqrt{3}\sigma_v/c_s$  (assuming isotropy), where  $c_s = \sqrt{kT_{\text{kin}}/\mu m_{\text{H}}}$  is the gas sound speed,  $k$  is the Boltzmann constant,  $\mu$  is the mean molecular weight of the gas, and  $m_{\text{H}}$  is the mass of a Hydrogen atom. We assume a mean molecular weight of  $\mu = 2.33$  (e.g. Kauffmann et al. 2008). Each individual model is therefore defined by a unique set of  $n_0$ ,  $\sigma_v$ ,  $T_{\text{kin}}$ , and  $\alpha_{\text{PL}}$ . We discuss how we set each of these parameters below.

### 2.3.1. Turbulent gas velocity dispersion, $\sigma_v$ :

In Paper I, we selected a model parameter space such that the median  $\Sigma_{\text{mol}} - \sigma_v$  trend generally followed the  $\Sigma_{\text{mol}} - \sigma_v$  fit to PHANGS data in Sun et al. (2018) and Milky Way cloud-scale studies (Heyer et al. 2009; Field et al. 2011). In this paper, we use cloud-scale ( $r = 40 - 45$  pc) measurements of cloud properties derived from observations of the CO  $J = 2 - 1$  line from the PHANGS sample (Sun et al. 2020), NGC3256 (Brunetti et al. 2021) and the Antennae (NGC4038/9) (Brunetti et al. 2024) as the basis of our model parameter space. We randomly sample measurements from each of these cloud-scale studies, that include pairs of molecular gas surface density and velocity dispersion,  $\Sigma_{\text{mol}}$  and  $\sigma_v$ . Constructing our model parameter space this way ensures that our models include representatives of cloud-scale observations of normal galaxies (from PHANGS), as well as more extreme systems that are representative of merging galaxies in our study (i.e. NGC3256 and the Antennae). The Antennae and NGC3256 are both in our lower-resolution sample from Paper I and this paper. We plot the corresponding cloud coefficients ( $\sigma_v^2/R$  vs.  $\Sigma_{\text{mol}}$ , where  $R$  is the size of the molecular component of the cloud, Heyer & Dame 2015; Field et al. 2011) of our model parameter space in comparison to those from the PHANGS sample (Sun et al. 2020) and those from our lower-



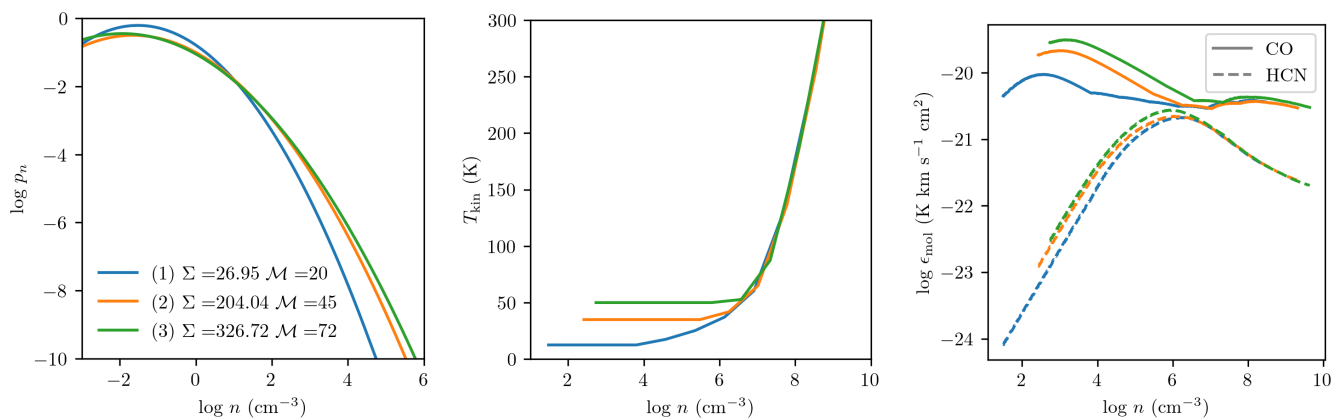


**Fig. 1.** *Left:* Example  $n - \text{PDFs}$  from our model parameter space assuming  $\alpha_{\text{PL}} = 3$ . We have picked three models that are representative of clouds in (1) the PHANGS sample (NGC 2903), (2) NGC 4038/9, and (3) NGC 3256. *Center:* Temperature profiles of the example models. *Right:* Emissivity profiles of the example models. CO emissivity is shown as the solid lines, and HCN emissivity is shown as the dashed lines. Note that the mass-weighted emissivity,  $\langle \epsilon_{\text{mol}} \rangle$ , is given by Eq. 11. The range of densities over which radiative transfer is applied is slightly different between models, and depends on the average gas surface density of the model (see section 2.3). We note that we plot  $p_n$  over a wider range of volume densities (left plot) than those used when performing radiative transfer (center and right plots).

resolution study ( $\sim 50 - 900$  pc, see Table 1 in Paper I) in Fig. 2.

Setting our model parameter space this way relies on the assumption that the CO velocity dispersion tracks the turbulent velocity dispersion at these scales. In Appendix A, we discuss in detail the uncertainties and evidence for use of observational estimates of gas velocity dispersion from molecular line emission, and summarize the main points here. Using simulations, Szűcs et al. (2016) find the measured  $^{12}\text{CO}$  velocity dispersion is within  $\sim 30 - 40\%$  of the turbulent 1D velocity dispersion in their cloud simulations, on average, and argue that the CO velocity dispersion should trace the turbulent velocity dispersion. This is smaller than the expected uncertainty on the mass conversion factor (Szűcs et al. 2016; Bolatto et al. 2013), which is up to a factor of two. Additionally, a weak correlation has been observed between mach number estimated from various molecular line transitions and gas density variance in resolved clouds in the Milky Way (e.g. Padoan et al. 1997; Brunt 2010; Ginsburg et al. 2013; Kainulainen & Tan 2013; Federrath et al. 2016b; Menon et al. 2021; Marchal & Miville-Deschênes 2021; Sharda & Krumholz 2022), although there is significant scatter potentially due to uncertainties in  $b$  (Kainulainen & Federrath 2017).

We cannot exclude the possibility of large-scale motions impacting the measured velocity dispersions of studies at 45-50 pc. For example, Federrath et al. (2016b) use HNC to estimate turbulent velocity dispersion in G0.253+0.016 (The Brick) and subtract a large-scale gradient that appears to contribute  $\sim 40 - 50\%$  of the measured velocity dispersion, possibly from shear due to its location in the CMZ of the Milky Way. Using the velocity profiles derived from Lang et al. (2020), we conclude that a small fraction of clouds in the PHANGS sample will be impacted by shear motions towards the centres of these disk galaxies (with contributions  $> 50\%$  to the measured velocity dispersion). It is more difficult to quantify the large-scale motions of gas within the mergers NGC 3256 and NGC 4038/9. Gas streaming motions or shear may bias measured velocity dispersions towards larger values (Sun et al. 2020; Henshaw et al. 2016; Federrath et al. 2016a). In general, the measured velocity dispersions are larger in the mergers; however, the gas density PDF is also expected to be wider in mergers (with more dense gas) due to enhanced compressive turbulence (cf. Renaud et al. 2014). Thus, we con-

clude that the velocity dispersion measurements from CO are likely track the turbulent velocity dispersion, and quote a typical uncertainty of 50%.

Finally, we note that clouds in the PHANGS sample and in NGC 3256 are marginally resolved at 40-45 pc scales (cf. Rosolowsky et al. 2021; Brunetti & Wilson 2022), and we expect the Antennae to have cloud sizes intermediate between those found in the PHANGS galaxies and NGC 3256. For comparison, a typical size of clouds in the Milky Way is 30 pc, with a large range from  $< 1$  pc to 100 pc (Miville-Deschênes et al. 2017). Thus, there will be some variation in how resolved each cloud is in the three studies we take measurements from (Sun et al. 2020; Brunetti et al. 2021, 2024). However, we do not expect molecular velocity dispersions in the galaxies to be significantly impacted by observational effects such as beam smearing, since the systems studied are relatively face on (Sun et al. 2020; Brunetti et al. 2021, 2024). Additionally, the *gas density variance - mach number relation* (cf. Eq. 3) will hold on scales smaller than the cloud size, since turbulence is expected to produce self-similar structure (e.g. Elmegreen & Scalo 2004; Dib et al. 2008; Burkhardt et al. 2013).

### 2.3.2. Mean gas density, $n_0$ :

We derive a mean gas density,  $n_0$ , based on the molecular gas surface density estimates,  $\Sigma_{\text{mol}}$ . We estimate a minimum mean gas density by converting  $\Sigma_{\text{mol}}$  to a volume density assuming a spherical geometry ( $n(R)$ , where  $R$  is the assumed size of the molecular cloud that is set by the pixel size), such that  $n_0 = \Sigma/R$ . We note that we also considered different prescriptions for calculating mean gas density based on the assumption of energy equipartition (i.e. fixed virial parameter) and dynamical equilibrium in a gas disk (Wilson et al. 2019). We find similar results regardless of the prescription we choose for  $n_0$  and therefore only present the results assuming  $n_0 = \Sigma/R$ .<sup>2</sup> We also acknowledge that the  $\Sigma_{\text{mol}}$  measurements from these cloud scale studies are still prone to uncertainties in CO conversion factor. However, we are able to confirm that our modeled CO  $J = 1 - 0$  intensi-

<sup>2</sup> On larger scales ( $\sim 1$  kpc), Bacchini et al. (2019) find  $n_0 \propto \Sigma^{0.6}$  in nearby spiral galaxies, however on these scales the contribution from HI becomes significant.

ties with  $I_{\text{CO}}$  are consistent with the intensities measured in our lower resolution sample (see Fig. 3), with only small offsets.

### 2.3.3. Power law slope of the $n$ – PDF, $\alpha_{\text{PL}}$ :

We aim to capture observed star formation scaling relations in our study, in addition to capturing observed cloud properties. Following Paper I, we use the gravo-turbulent models of star formation from Burkhardt (2018) and Burkhardt & Mocz (2019), which assume the  $n$  – PDF is a combination of a lognormal turbulence-dominated component and gravity-dominated powerlaw tail at high densities. We use these models to estimate  $\epsilon_{\text{ff}} = t_{\text{dep}}/t_{\text{ff}}$  (star formation efficiency per free-fall time),  $t_{\text{dep}}$ , and  $\Sigma_{\text{SFR}}$  (the star formation rate surface density). Table 2 in Paper I describes how each of these quantities are derived. In this framework, the choice of  $\alpha_{\text{PL}}$  (the slope of the power law component of the  $n$  – PDF in the gravoturbulent star formation models of Burkhardt 2018; Burkhardt & Mocz 2019) has an impact on the resulting  $\epsilon_{\text{ff}}$  such that steeper  $\alpha_{\text{PL}}$  values result in higher  $\epsilon_{\text{ff}}$  and vice versa. We choose  $\alpha_{\text{PL}} = 3$  as our fiducial value (which corresponds to  $k = 1.5$ , see Eq. 8).<sup>3</sup> Similar to Paper I, we must also assume a local efficiency of  $\epsilon_0$  so that values of  $t_{\text{dep}}$  and  $\Sigma_{\text{SFR}}$  derived from our models are consistent with observations.  $\epsilon_0$  accounts for a reduction in star formation efficiency from stellar feedback processes. For  $\alpha_{\text{PL}} = 3$  we take  $\epsilon_0 = 0.01$ , which returns  $\epsilon_{\text{ff}} \approx 0.01 - 0.1$ , and is consistent with expectations from observations and simulations (e.g., Salim et al. 2015; Utomo et al. 2018; Sharda et al. 2018; Hu et al. 2022b).

### 2.3.4. Gas kinetic temperature, $T_{\text{kin}}$ :

We estimate  $T_{\text{kin}}$  following the prescription in Sharda & Krumholz (2022), which assumes thermal equilibrium balance of heating and cooling processes in the presence of protostellar radiation feedback:

$$\Gamma_c + \Gamma_{\text{CR}} + \Gamma_{\text{H}_2} + \Psi_{\text{gd}} + \Lambda_{\text{M}} + \Lambda_{\text{H}_2} + \Lambda_{\text{HD}} = 0. \quad (4)$$

This equation includes compressional heating ( $\Gamma_c$ ), cosmic ray heating ( $\Gamma_{\text{CR}}$ ),  $\text{H}_2$  formation heating ( $\Gamma_{\text{H}_2}$ ), metal line cooling ( $\Lambda_{\text{M}}$ ),  $\text{H}_2$  cooling ( $\Lambda_{\text{H}_2}$ ), and hydrogen deuteride cooling ( $\Lambda_{\text{HD}}$ ), as well as the dust-gas energy exchange ( $\Psi_{\text{gd}}$ ), which can serve as either a cooling or heating process. The Sharda & Krumholz (2022) prescription includes feedback from active star formation in a semi-analytical framework. In addition to aforementioned cooling and heating mechanisms, Sharda & Krumholz (2022) consider the impact of radiation feedback from existing protostars in the cloud via the dust-gas energy exchange term, where the dust temperature is set by radiation feedback from active star formation. This prescription is adopted from Chakrabarti & McKee (2005) where the authors developed a framework to treat dust temperatures in the presence of a central radiating source (see also, Krumholz 2011).

We adopt the prescription for cosmic ray heating from Krumholz et al. (2023) that is based on the gas depletion time. Krumholz et al. (2023) estimate the average cosmic ray ionization rate,  $\zeta_{\text{CR}}$ , to be:

$$\zeta_{\text{CR}} = 1 \times 10^{-16} \left( \frac{t_{\text{dep}}}{\text{Gyr}} \right)^{-1} \text{ s}^{-1}. \quad (5)$$

The cosmic ray heating rate is then:

$$\Gamma_{\text{CR}} = q_{\text{CR}} \zeta_{\text{CR}} \quad (6)$$

<sup>3</sup> For comparison to the power law slopes of  $p_s$  in Paper I, subtract one from  $\alpha_{\text{PL}}$ .

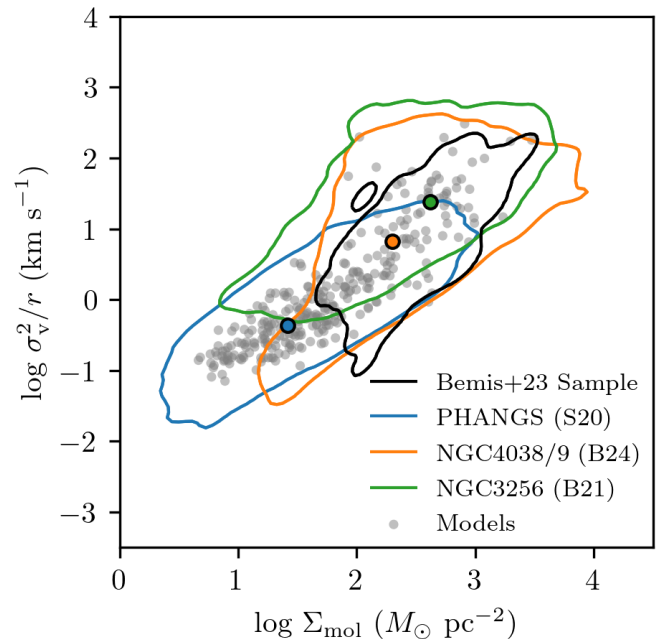


**Fig. 2.** The model points are plotted as the gray points in the  $\sigma_v^2/R - \Sigma_{\text{mol}}$  parameter space, and include a mix of cloud measurements from the PHANGS sample (Sun et al. 2020), NGC4038/9 (Brunetti et al. 2024), and NGC3256 (Brunetti et al. 2021). We also outline  $\sigma_v^2/R - \Sigma_{\text{mol}}$  measurements of the Sun et al. (2020) PHANGS galaxies at 90 pc resolution ( $r = 45$  pc, blue contours), NGC4038/9 at 80 pc resolution ( $r = 40$  pc, orange contours), and NGC3256 at 80 pc resolution ( $r = 40$  pc, green contours). The lower resolution data from Paper I are outlined by the black solid line. Example models from Fig. 1 are indicated in this plot as the blue (1), orange (2), and green (3) points.

where we take the average energy per ionization to be  $q_{\text{CR}} = 12.25$  eV, which is appropriate for molecular gas (Wolfire et al. 2010). We use  $t_{\text{dep}}$  estimates that are consistent with the molecular gas star formation laws found by Bigiel et al. (2008) and Wilson et al. (2019). The original prescription used by Sharda & Krumholz (2022) from Crocker et al. (2021) overestimates the gas temperature for molecular clouds.

In addition to these processes included in Sharda & Krumholz (2022), we also incorporate mechanical heating:

$$\Gamma_{\text{turb}} = 3.3 \times 10^{-27} \frac{n \sigma_v^3}{R} \text{ erg cm}^{-3} \text{ s}^{-1} \quad (7)$$

which is potentially important for more turbulent clouds (Pan & Padoan 2009; Ao et al. 2013), such as those in mergers or at the centers of barred galaxies. We find that on average over the cloud model, turbulent heating dominates in the models using NGC4038/9 and NGC3256 gas surface density and velocity dispersion measurements, while cosmic ray heating dominates in the models using gas surface density and velocity dispersion measurements from PHANGS galaxies. We show example temperature profiles for average PHANGS, NGC4038/9, and NGC3256 models in Fig. 1. For low density regions near the exterior of the model clouds, the heating/cooling model sometimes produces temperature increases, which are likely unphysical. At these low densities we fix the temperature to the minimum value over the model cloud (Fig. 1). We note that we assume a Solar metallicity composition of the gas for all our cloud models for simplicity, ignoring the metallicity dependence of  $T_{\text{kin}}$ .

## 2.4. Applying Radiative Transfer

We use RADEX (van der Tak et al. 2007) to perform radiative transfer and calculate emissivities of our cloud models. Each cloud model is comprised of an  $n$ -PDF distribution with 500 resolution elements across the PDF in volume density. We run RADEX at each resolution element across the  $n$ -PDF, using the escape probability formulation and adopting its default uniform sphere geometry. For each resolution element in our cloud model, RADEX computes a line flux, optical depth, and excitation temperature that we later use to calculate PDF-averaged properties of each cloud model (see section 2.4.1). To perform its radiative transfer calculation, RADEX requires the input of  $H_2$  volume density, molecular column density, gas kinetic temperature, and molecular line width at each resolution element. In section 2.3 we describe how we set fiducial values of mean gas density,  $n_0$ , velocity dispersion  $\sigma_v$ , and kinetic temperature,  $T_{\text{kin}}$  for each individual model across our model parameter space. We describe how these physical inputs translate to the range of volume and column densities required for each model in the paragraphs below.

To provide RADEX with a molecular column density for each volume density in the model, we assume a power law density distribution for the  $H_2$  volume ( $n_{H_2}$ ) and column ( $N_{H_2}$ ) density distributions. One zone models bypass this requirement by assuming a fixed optical depth (e.g. Leroy et al. 2017b), which indirectly determines the  $n - N$  relationship, but can underestimate molecular abundances at high densities, and overestimate them at low densities. We therefore adopt power law radial density distributions that are more realistic for molecular clouds. Spatial density gradients are observed in real molecular clouds, and the slopes of spatial density gradients are potentially connected to the shape of their  $n - \text{PDF}$  (cf. Federrath & Klessen 2013). Furthermore, these slopes are likely connected to the star formation properties of molecular clouds (Tan et al. 2006; Elmegreen 2011; Parmentier 2014; Kainulainen et al. 2014; Parmentier 2019). The Burkhart (2018) and Burkhart & Mocz (2019) models predict a connection between the power law slope of the  $n - \text{PDF}$  and  $\epsilon_{\text{ff}}$ , and this behaviour has also been observed in Milky Way clouds (Federrath & Klessen 2013). We therefore use the power law slope of the  $n - \text{PDF}$  of our models,  $\alpha_{\text{PL}}$ , to determine the gas density gradient of our models.

Federrath & Klessen (2013) show that the slope of the gradient in a radially-symmetric density distribution will be related to the slope of the corresponding  $n - \text{PDF}$  if they both follow power law scalings. Using this scaling for spherical geometries in Federrath & Klessen (2013), we connect the slope of the high-density power law tail of the  $n - \text{PDF}$  ( $\alpha_{\text{PL}}$ ) to the radial slope of the clump density profile,  $k$ , via (cf. Federrath & Klessen 2013):

$$k = \frac{3}{\alpha_{\text{PL}} - 1}. \quad (8)$$

For comparison, a power law with  $k = 2$  is consistent with the expectation for isothermal cores (Shu 1977), and results in an  $n - \text{PDF}$  slope of  $\alpha_{\text{PL}} = 2.5$ . Shallower  $n - \text{PDF}$  slopes then correspond to steeper spatial density gradients and vice versa.

The radially-symmetric approximation assumed above is only analytically exact for the gravitationally-bound gas in the power law tail of the  $n - \text{PDF}$ . The gas outside of the power law tail is primarily governed by turbulence, which produces fractal, self-similar structure (e.g. Elmegreen & Falgarone 1996; Schneider et al. 2011). Self-similarity implies there is no characteristic scale of the gas, but this is not inconsistent with the existence

of density gradients in turbulent gas. In the interest of simplicity we also adopt the same power law density gradient for the gas that we attribute to the lognormal component of the  $n - \text{PDF}$ . We implement this by adopting a power law for the radial volume and column density distributions, normalised to surface values (see Eqs. 9 and 10, respectively.) The radial volume density distribution is then given by:

$$n(r) = n(R) \left( \frac{r}{R} \right)^{-k} \quad (9)$$

where  $r$  is the radial coordinate,  $R$  is the size of the molecular component of the cloud, and  $n(R)$  is the volume density of the molecular cloud. We assume that, in general, the radial profile of the column density will track the radial profile of the volume density. This general trend is consistent with the assumption of either a stiff equation of state (temperature increases with density), as well as an isothermal equation of state (Federrath & Banerjee 2015). The gas-temperature relationship in our models is, on average, consistent with a stiff equation of state. Since the exact trend varies from model to model, we simply adopt:

$$N(r) = N(R) \left( \frac{r}{R} \right)^{-(k-1)} \quad (10)$$

where  $N(R)$  is the column density at the surface of the molecular cloud and is consistent with an isothermal cloud following and ideal gas equation of state. We then derive molecular column density distributions by multiplying the radial  $H_2$  column density distribution (Eq. 10) by the appropriate absolute molecular abundance. Although abundance variations are possible within our sources, we present the results of our models assuming fixed molecular abundances  $x_{\text{HCN}} = 10^{-8}$  and  $x_{\text{CO}} = 1.4 \times 10^{-4}$  relative to  $H_2$  when converting  $N_{H_2}$  to a molecular column density, i.e.  $N_{\text{HCN}}$  or  $N_{\text{CO}}$  (Draine 2011). We show example emissivity profiles for several models in Fig. 1. We note that we assume fixed abundances so that the results of our modelling focus on the impact of variations in turbulent velocity dispersion on HCN and CO emissivities. We run additional models to assess the impact of varying the absolute abundance of HCN and CO on model output, and we present these results in Appendix B. In summary, we find that variations in molecular abundance have a moderate impact on the optical depths of HCN and CO emission, but that these variations do not significantly impact the various correlations between HCN, CO, and molecular cloud properties considered in this work.

### 2.4.1. Deriving Emissivity and Intensity from Molecular Cloud Models

Using the framework described in sections 2.1 – 2.4, we numerically solve for CO and HCN  $J = 1 - 0$  emissivities. Similar to Leroy et al. (2017b), we weight the unintegrated emissivities (Eq. 1) by the mass distribution of model clouds,  $p_n$ , and integrate to determine the mass-weighted emissivity,

$$\langle \epsilon_{\text{mol}} \rangle = \frac{\int \epsilon_{\text{mol}}(n) n p_n \text{d}n}{\int n p_n \text{d}n} \quad (11)$$

where we have re-written Eq. 1 in terms of  $n$ . When calculating  $\langle \epsilon_{\text{mol}} \rangle$ , we numerically integrate the PDF over densities that are relevant to molecular gas, roughly  $\sim 10 - 10^8 \text{ cm}^{-3}$ . This produces a mass-averaged molecular line emissivity with units of  $\text{K km s}^{-1} \text{ cm}^2$ . As Leroy et al. (2017b) point out,  $1 / \langle \epsilon_{\text{mol}} \rangle$  can



be recast in units of  $M_{\odot}/\text{pc}^2 [\text{K km s}^{-1}]^{-1}$ , similar to a molecular line luminosity-to-mass conversion factor. We note that in this work we primarily model quantities that are *surface densities*, i.e. molecular intensity and column density. However, we are still able to compare the relative mass conversion factors of HCN and CO using properties of the  $n$ -PDF, and we explore the difference between emissivity and conversion factors more in section 3.2.

Similar to Eq. 1, the modelled emissivity can be parameterized by an averaged intensity,  $\langle I_{\text{mol}} \rangle$ , and an average column density,  $\langle N_{\text{H}_2, \text{mol}} \rangle$ , over which the transition is sensitive to, i.e.:  $\langle \epsilon_{\text{mol}} \rangle = \langle I_{\text{mol}} \rangle / \langle N_{\text{H}_2, \text{mol}} \rangle$ . Thus, if we know  $\langle N_{\text{H}_2, \text{mol}} \rangle$ , we can derive intensities that are analogous to what are measured in observations of individual molecular clouds. We estimate the average column of mass that a transition is sensitive to,  $\langle N_{\text{H}_2, \text{mol}} \rangle$ , from our models using:

$$\langle N_{\text{H}_2, \text{mol}} \rangle = \frac{\int N_{\text{H}_2}(n) \epsilon_{\text{mol}}(n) n p_n \, dn}{\int \epsilon_{\text{mol}}(n) n p_n \, dn} \quad (12)$$

where  $N_{\text{H}_2}(n)$  is the  $\text{H}_2$  column density corresponding to  $\text{H}_2$  volume density  $n$ , and the two quantities are related via Eqs. 9 and 10 in our models. Using  $\langle N_{\text{H}_2, \text{mol}} \rangle$ , we derive intensities from our emissivities that can be compared with those measured in our sample from Paper I and the EMPIRE sample (Jiménez-Donaire et al. 2019).

RADEX also returns optical depth and excitation temperature for a given molecular transition at each  $n$  across the  $n$ -PDF. We determine a fiducial optical depth,  $\langle \tau_{\text{mol}} \rangle$ , and excitation temperature,  $\langle T_{\text{ex, mol}} \rangle$ , for a given molecular transition of each cloud model by calculating the expectation values of these quantities weighted by emissivity via:

$$\langle \tau_{\text{mol}} \rangle = \frac{\int \tau_{\text{mol}}(n) \epsilon(n) n p_n \, dn}{\int \epsilon(n) n p_n \, dn}, \text{ and} \quad (13)$$

$$\langle T_{\text{ex, mol}} \rangle = \frac{\int T_{\text{ex, mol}}(n) \epsilon(n) n p_n \, dn}{\int \epsilon(n) n p_n \, dn}. \quad (14)$$

These estimates of  $\tau_{\text{mol}}$  and  $T_{\text{ex, mol}}$  are useful for comparison to observations.

### 3. Model Results

We present the model results in the following sections in Figs. 3 to 10. In section 3.1 we discuss the impact of excitation and optical depth on the modelled CO and HCN intensities and illustrate these results using the first set of plots (Figs. 3, 4, 5). We constrain the characteristic gas densities that the HCN/CO ratio is sensitive to in section 3.2 (cf. Fig. 6). We explore trends in the CO and HCN emissivity ( $\langle \epsilon_{\text{CO}} \rangle$  and  $\langle \epsilon_{\text{HCN}} \rangle$ ) and luminosity-to-mass conversion factors ( $\alpha_{\text{CO}}$  and  $\alpha_{\text{HCN}}$ , cf. Fig. 7) in section 3.3. In sections 3.4 and 3.5, we explore if the  $I_{\text{HCN}}/I_{\text{CO}}$  ratio traces the fraction of gravitationally-bound gas (section 3.4), as well as how variations in CO and HCN emissivity impact our interpretation of star formation scaling relations (section 3.5). We note that we sometimes differentiate between models that represent clouds from different star forming regimes, i.e. PHANGS-type vs. NGC3256-type and NGC4038/9-type, and color the results presented in some figures accordingly.

In sections 3.2, 3.4, and 3.5, we combine the predictions of the LN+PL analytical models of star formation (Burkhart 2018)

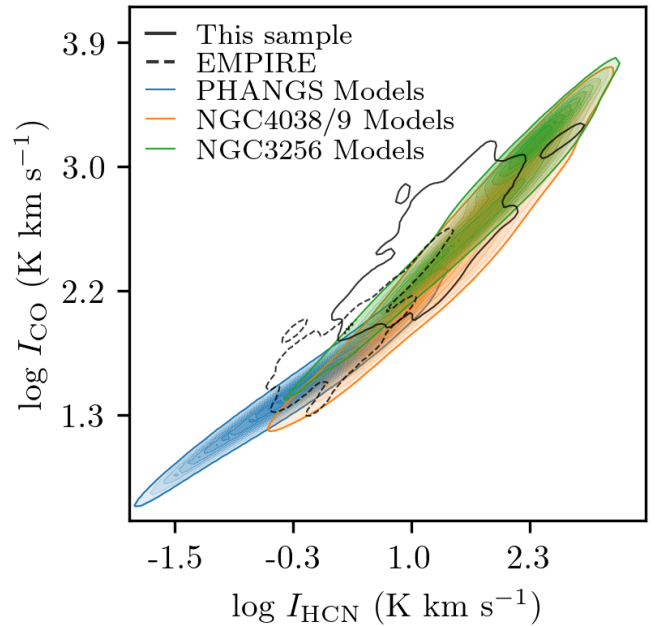


**Fig. 3.** Modelled  $I_{\text{CO}}$  and  $I_{\text{HCN}}$  compared with the measured intensities of the Paper I sample (solid contours) and the EMPIRE sample (dashed contours Jiménez-Donaire et al. 2019). Blue filled contours are models whose  $\Sigma$  and  $\sigma_v$  are taken from the PHANGS sample (Sun et al. 2020), orange filled contours are those taken from NGC 4038/9 (Brunetti et al. 2024), and green filled contours are those taken from NGC 3256 (Brunetti et al. 2021). Ten contours are drawn in even steps from the 16<sup>th</sup> to 100<sup>th</sup> percentile.

with the results of our radiative transfer modelling. For convenience, we produce a summary of the most relevant equations in the bottom of Table 2 in Paper I describing how various quantities are calculated. In these sections we explore how variations in CO and HCN emissivity, as well as variations in the CO and HCN luminosity-to-mass conversion factors, may impact observed star formation scaling relations. We mimic the results of observational studies by applying common conversion factors to our modelled molecular line intensities to derive gas surface densities (method 1), and we compare these results with the true model predictions (method 2). For method 1, the modelled molecular intensities are multiplied by constant conversion factors, as we have done with our sample from Paper I and the EMPIRE sample. We choose a value that is intermediate between the Milky Way and starburst values for  $\alpha_{\text{CO}}$ :  $\alpha_{\text{CO}} = 3 [M_{\odot} (\text{K km s}^{-1} \text{pc}^2)^{-1}]$  and  $\alpha_{\text{HCN}} = 3.2 \alpha_{\text{CO}}$  to produce estimates of gas mass surface densities, which are the same values used in Paper I.

#### 3.1. Excitation and Optical Depth

We show the modelled CO and HCN intensities compared to the intensities measured in our sample from Paper I and the EMPIRE sample from (Jiménez-Donaire et al. 2019) in Fig. 3. The ranges of HCN and CO  $J = 1 - 0$  intensities produced by our models encompass those we measure in the disk galaxies of the EMPIRE sample ( $I_{\text{HCN}} = 0.4 - 20.5 \text{ K km s}^{-1}$  and  $I_{\text{CO}} = 21.6 - 331.5 \text{ K km s}^{-1}$ , Jiménez-Donaire et al. 2019) and our more extreme sample of galaxies including U/LIRGs and galaxy centers ( $I_{\text{HCN}} = 0.8 - 814.5 \text{ K km s}^{-1}$  and  $I_{\text{CO}} = 53.8 - 2397.4 \text{ K km s}^{-1}$ , Bemis & Wilson 2023, cf. Fig. 3).

The scatter is less well-matched to observations, which may be due to uncertainties in the relative filling fractions of HCN and CO. We calculate the median absolute deviations (MAD) of our measured and modelled HCN and CO intensities and multiply by 1.4826 to get an estimate of the scatter (standard deviation) that is less sensitive to outliers. We find scatters of  $\sigma_{\text{HCN}} = 1.9 \text{ K km s}^{-1}$  and  $\sigma_{\text{CO}} = 27.2 \text{ K km s}^{-1}$  for the EMPIRE sample,  $\sigma_{\text{HCN}} = 13.2 \text{ K km s}^{-1}$  and  $\sigma_{\text{CO}} = 176.2 \text{ K km s}^{-1}$  for our sample, and  $\sigma_{\text{HCN}} = 3.2 \text{ K km s}^{-1}$  and  $\sigma_{\text{CO}} = 51.2 \text{ K km s}^{-1}$  for all models. We find scatters of HCN and CO intensity for just the PHANGS-type models to be  $\sigma_{\text{HCN}} = 1.2 \text{ K km s}^{-1}$  and  $\sigma_{\text{CO}} = 25.0 \text{ K km s}^{-1}$ , which is well-matched to the observations of the EMPIRE sample. In contrast to this, we find  $\sigma_{\text{HCN}} = 64.0 \text{ K km s}^{-1}$  and  $\sigma_{\text{CO}} = 500.0 \text{ K km s}^{-1}$  for the NGC4038/9 and NGC3256 models combined. This scatter is less well-matched to our data, although roughly on the same order of magnitude as what is measured in our sample. We discuss the impact of emissivity on the scatter of observations in section 3.5.

Figure 4 presents the model CO and HCN  $J = 1 - 0$  intensities as a function of the excitation temperature and optical depth. We find that the CO  $J = 1 - 0$  transition is close to LTE for the majority of our models when compared to our estimates of  $\langle T_{\text{kin}} \rangle$ . A subset of PHANGS models show slightly subthermal emission, which is due to the average density of these models being below the critical density for CO  $J = 1 - 0$  (i.e.  $\sim 10^{2-3} \text{ cm}^{-3}$ ), the density at which the majority of CO emission becomes thermalised. The CO  $J = 1 - 0$  transition is, on average, optically thick for the PHANGS-type models. Towards higher  $I_{\text{CO}}$  where the models are dominated by NGC4038/9- and NGC3256-type clouds, the CO optical depth drops and approaches  $\tau \sim 1$  towards the models with the brightest CO emission. This behavior is similar to the results of previous studies of CO excitation (e.g. Narayanan & Krumholz 2014), where the optical depth of the  $J = 1 - 0$  transition appears to drop towards gas where CO is more excited (and  $\Sigma_{\text{SFR}}$  is high). This is due to the fact that the optical depth of CO  $J = 1 - 0$  is inversely proportional to velocity dispersion, and that velocity dispersion tends to increase with  $\Sigma_{\text{SFR}}$ .

The HCN  $J = 1 - 0$  transition appears subthermally excited, which agrees with a number of studies that assess the excitation of HCN in the Milky Way and nearby galaxies (e.g. Dame & Lada 2023; García-Rodríguez et al. 2023; Tafalla et al. 2023). The HCN optical depth is found to be only moderately optically thick for the PHANGS-type clouds in our models, and is in agreement with previous studies towards the centers of disk galaxies (Jiménez-Donaire et al. 2017). These results suggest that variations in  $I_{\text{CO}}$  may be more strongly impacted by variations in  $\tau_{\text{CO}}$  relative to the impact of  $\tau_{\text{HCN}}$  on  $I_{\text{HCN}}$ . We note that the drop in the CO optical depth for the extreme systems coincides with a transition in the dominant heating mechanism from cosmic ray heating to turbulent heating, and is a reflection of an increase in the typical gas velocity dispersion in NGC4038/9 and NGC3256-type clouds relative to PHANGS-type clouds.

We also explore how physical quantities impact CO and HCN  $J = 1 - 0$  intensities in our models. In Fig. 5, we present the model CO and HCN  $J = 1 - 0$  intensities as a function of mean density, velocity dispersion, kinetic temperature and gas surface density. We perform fits using orthogonal distance regression. We also calculate Spearman rank coefficients and show these in the lower right corner of each plot. For comparison, we have included the relationships between  $I_{\text{HCN}}/I_{\text{CO}}$  and  $\sigma_v$  and  $\Sigma_{\text{mol}}$  found in nearby galaxies from the ALMOND survey (Neumann et al. 2023), as well as the relationship found by Tafalla et al. (2023) between  $I_{\text{HCN}}/I_{\text{CO}}$  and gas surface density as deter-

mined through extinction measurements in Milky Way clouds. Both  $I_{\text{HCN}}$  and  $I_{\text{CO}}$  are strongly correlated with  $n_0$ ,  $\sigma_v$ , and  $\langle T_{\text{kin}} \rangle$ . We also fit each trend to assess how rapidly  $I_{\text{HCN}}$  and  $I_{\text{CO}}$  change with each parameter. We find that  $I_{\text{HCN}}$  increases more steeply than  $I_{\text{CO}}$  with each parameter. Individually,  $I_{\text{CO}}$  and  $I_{\text{HCN}}$  are most strongly correlated with the velocity dispersion, with the ratio  $I_{\text{HCN}}/I_{\text{CO}}$  instead appearing most strongly correlated with the mean density. The trend in  $I_{\text{HCN}}/I_{\text{CO}}$  vs.  $\sigma_v$  is more shallow for the ALMOND galaxies than what is found by our models. The trend from ALMOND galaxies intersects with the NGC 3256- and NGC 4038/8-type models relative to the PHANGS-type models. In general, there appears to be slight differences between the PHANGS-type clouds to NGC4038/9- and NGC3256-type clouds in how  $I_{\text{HCN}}$  and  $I_{\text{CO}}$  vary with each physical parameter. This is most obvious when looking at the ratio of  $I_{\text{HCN}}/I_{\text{CO}}$  relative to each quantity. Most notably, the trends in  $I_{\text{HCN}}/I_{\text{CO}}$  with  $n_0$ ,  $\sigma_v$ , and  $\langle T_{\text{kin}} \rangle$  appear to flatten towards the NGC4038/9- and NGC3256-type models (relative to the PHANGS-type models).

We also find a relationship between  $I_{\text{HCN}}/I_{\text{CO}}$  and gas surface density in our models (cf. 5), which has been found in studies of gas clouds in the Milky Way (e.g. Tafalla et al. 2023) as well as nearby galaxies (e.g. Gallagher et al. 2018a; Neumann et al. 2023). We perform a fit between  $\log(I_{\text{HCN}}/I_{\text{CO}})$  and  $\log$  of the mean gas surface density and find a sublinear relationship similar to that found by Tafalla et al. (2023, eq. 6):

$$\log\left(\frac{I_{\text{HCN}}}{I_{\text{CO}}}\right) = (0.81 \pm 0.03) \log\left(\frac{\Sigma_{\text{mol}}}{M_{\odot} \text{ pc}^{-2}}\right) - 2.73_{-0.08}^{+0.07}. \quad (15)$$

Uncertainties on the fit are determined using bootstrapping. Tafalla et al. 2023 find a slope of 0.71. As Tafalla et al. (2023) show, other extragalactic studies find sublinear slopes, as well (0.81 in Gallagher et al. 2018b and 0.5 in Jiménez-Donaire et al. 2019). Interestingly, the recent results of the ALMOND survey find a much shallower slope of  $\sim 0.33$  (Neumann et al. 2023). Neumann et al. (2023) compare observations of HCN and CO at 2.1 kpc scales with cloud-scale measurements of velocity dispersion and gas surface density from PHANGS galaxies, which may explain this discrepancy. We compare our fit with the results of Tafalla et al. (2023) and Neumann et al. (2023) in Fig. 5. Our fit is slightly offset from Tafalla et al. (2023), which is consistent with the offset we see in our model intensities in Fig. 3. This relationship is in part due to the gas volume density and gas surface density scaling with each other in our models (cf. Eqs. 9 and 10), and the overall dense gas fraction increasing with gas volume density.<sup>4</sup> In general, our models are able to reproduce the sublinear relationship observed between the HCN/CO intensity ratio and gas surface density observed in both Milky Way clouds at  $\sim \text{pc}$  scales and nearby galaxies at  $\sim \text{kpc}$  scales.

In summary, our models are able to reproduce the range of HCN and CO  $J = 1 - 0$  intensities measured in the disk galaxies of the EMPIRE sample (Jiménez-Donaire et al. 2019) and our more extreme sample of galaxies including U/LIRGs and galaxy centers, presented in Paper I (cf. Fig. 3). Furthermore, we show that our models reproduce the expectations of CO excitation and optical depth (cf. Bolatto et al. 2013; Narayanan et al. 2012; Narayanan & Krumholz 2014). Although HCN is less well-studied than CO, we find that our models agree with results of the current works. In particular, HCN appears subthermally excited, as has been found via studies of high- $J$  lines of HCN emission in nearby galaxies (García-Rodríguez et al.

<sup>4</sup> We note that simulations find that gas volume density tracks column densities in molecular clouds (cf. Priestley et al. 2023).



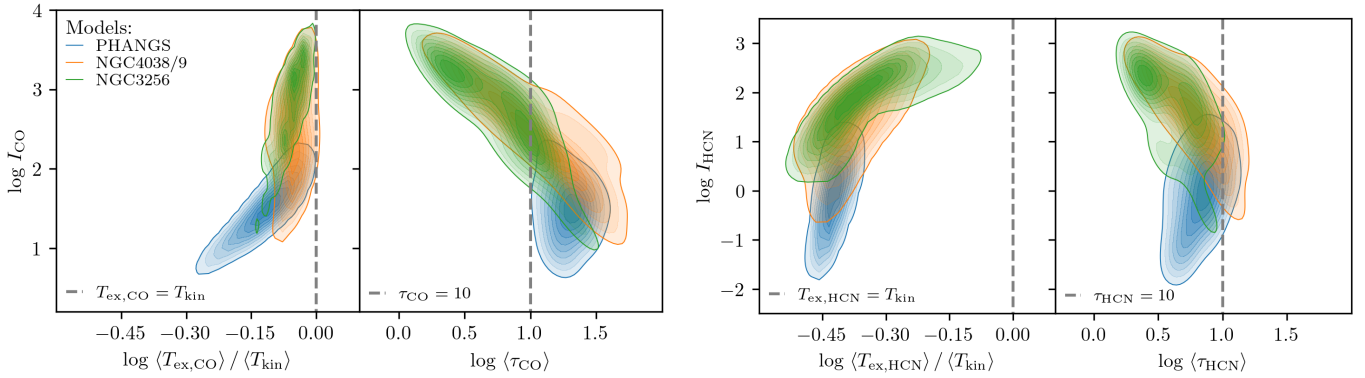


**Fig. 4.** Correlations between modelled  $I_{\text{CO}}$  (left two plots) and  $I_{\text{HCN}}$  (right two plots) and their respective excitation temperatures and optical depths determined using Eqs. 13 and 14. Formatting is the same as in Fig. 3. We find that CO optical depth decreases with increasing  $I_{\text{CO}}$  and CO excitation, in general agreement with the findings of previous studies (e.g. Bolatto et al. 2013; Narayanan et al. 2012; Narayanan & Krumholz 2014). In our models, HCN appears subthermally excited and moderately optically thick, also in agreement with findings of previous studies (e.g. Dame & Lada 2023; Jiménez-Donaire et al. 2017).

2023), and inferred from studies in Milky Way clouds (Dame & Lada 2023). Additionally, HCN appears only moderately optically thick ( $\tau < 10$ ), as was found by (Jiménez-Donaire et al. 2017) when comparing HCN and  $\text{H}^{13}\text{CN}$  emission towards the centers of nearby disk galaxies. Since gas volume density tracks column density in our models, we find  $I_{\text{HCN}}/I_{\text{CO}}$  also scales with gas surface density.

### 3.2. The fraction of gas traced by the HCN/CO ratio

We consider what fraction of gas the  $I_{\text{HCN}}/I_{\text{CO}}$  ratio is sensitive to in molecular clouds, and whether this changes in more extreme environments, such as those found in galaxy centers. This is motivated by previous studies which have found an increase in the dense gas depletion time towards the centers of some disk galaxies (Gallagher et al. 2018b; Querejeta et al. 2019; Jiménez-Donaire et al. 2019; Bešlić et al. 2021) and even in the nuclei of the Antennae (Bemis & Wilson 2019), despite these regions also having higher  $I_{\text{HCN}}/I_{\text{CO}}$ . Under the assumption that  $I_{\text{HCN}}/I_{\text{CO}}$  tracks the fraction of dense ( $n > 10^{4.5} \text{ cm}^{-3}$ ), star-forming gas in molecular clouds, those results appeared in conflict with fixed threshold models of star formation that predict star formation should turn on above a relatively fixed density, and that the star formation rate should increase in the presence of higher  $f_{\text{dense}}$  (see the works by Usero et al. 2015; Khullar et al. 2019). In agreement with previous studies (e.g. Burkhardt & Mocz 2019), Paper I shows that gravoturbulent models of star formation are able to reproduce this increase in dense gas depletion time towards regions with higher fractions of dense gas. This result agrees with the findings of Gallagher et al. (2018b); Querejeta et al. (2019); Jiménez-Donaire et al. (2019); Bešlić et al. (2021) and Bemis & Wilson (2019). The major caveats of this conclusion are: 1. that  $I_{\text{HCN}}/I_{\text{CO}}$  is tracing the fraction of gas above a relatively fixed density (i.e.  $n > 10^{4.5} \text{ cm}^{-3}$ ), and 2. that the turbulent gas velocity dispersion is also increasing with  $I_{\text{HCN}}/I_{\text{CO}}$ . We have already shown that  $I_{\text{HCN}}/I_{\text{CO}}$  increases with  $\sigma_v$  in Fig. 5. We now consider if  $I_{\text{HCN}}/I_{\text{CO}}$  is tracing the fraction of gas above a relatively fixed density.

In Paper I, we focus on comparing the HCN/CO ratio with the fraction of gas above  $n > 10^{4.5} \text{ cm}^{-3}$ , which is the assumed threshold density for some clouds in the Milky Way disk. Other studies have shown that HCN is tracing gas primarily at moderate densities,  $n \sim 10^3 \text{ cm}^{-3}$  (e.g., Kauffmann et al. 2017; Pety

et al. 2017; Shimajiri et al. 2017; Barnes et al. 2020; Tafalla et al. 2021, 2023; Santa-Maria et al. 2023, Ngoc Le et al. in prep.), such that it may be more sensitive to mass fractions including densities below  $n \sim 10^{4.5}$ . We compare the modelled HCN/CO ratio to several gas fractions derived from the model  $n$ -PDFs in Fig. 6. To determine the fraction of gas above an arbitrary threshold density, we integrate the  $n$ -PDF above that threshold ( $n_{\text{thresh}}$ ):

$$f(n > n_{\text{thresh}}) = \frac{\int_{n > n_{\text{thresh}}} n p_n dn}{\int n p_n dn}. \quad (16)$$

We calculate gas fractions using the  $n$ -PDF above densities  $\log(n) = 2.5, 3.5, 4.5, 5.5 \text{ cm}^{-3}$ , denoted by  $f_{2.5}, f_{3.5}, f_{4.5}$ , and  $f_{5.5}$ , respectively. We numerically integrate over a wide range in densities when calculating these fractions to ensure the  $n$ -PDF is fully sampled. We note that we multiply the modelled  $I_{\text{HCN}}/I_{\text{CO}}$  ratio by a fixed factor,  $\alpha_{\text{HCN}}/\alpha_{\text{CO}} = 3.2$ , which is the ratio of the Gao & Solomon (2004a,b) HCN-to-dense  $\text{H}_2$  mass and Milky Way CO-to-total  $\text{H}_2$  mass conversion factors, and is the same factor we have applied to the HCN/CO ratio measured in the sources of our sample to estimate dense gas fractions in Paper I.

We calculate Spearman rank coefficients ( $r$ ) between  $I_{\text{HCN}}/I_{\text{CO}}$  and the gas fractions shown in Fig. 6 (i.e.  $f_{2.5}, f_{3.5}, f_{4.5}$ , and  $f_{5.5}$ ). The  $I_{\text{HCN}}/I_{\text{CO}}$  from our models is strongly ( $|r| > 0.7$ ) correlated with all of the gas fractions we consider, with little difference between their Spearman rank coefficients. We fit the correlations between  $3.2 \times I_{\text{HCN}}/I_{\text{CO}}$  and each of the fractions shown in Fig. 6 to assess the directness of each relationship. With a slope close to unity, the  $I_{\text{HCN}}/I_{\text{CO}}$  ratio appears to have the most direct relationship with the fraction of gas above  $n \sim 10^{3.5} \text{ cm}^{-3}$ . The relationship between  $3.2 \times I_{\text{HCN}}/I_{\text{CO}}$  and  $f(n > 10^{4.5} \text{ cm}^{-3})$  appears sublinear in our models, such that  $3.2 \times I_{\text{HCN}}/I_{\text{CO}}$  overestimates  $f(n > 10^{4.5} \text{ cm}^{-3})$  for the PHANGS-type clouds. These results suggest that  $I_{\text{HCN}}/I_{\text{CO}}$  is tracing gas above a relatively constant fraction of gas, but that this includes gas at moderate densities below  $n < 10^{4.5} \text{ cm}^{-3}$ .

In summary, our models predict that, on average,  $I_{\text{HCN}}/I_{\text{CO}}$  does appear to track gas above a relatively fixed density, but that this fraction includes more moderately dense gas (i.e.  $n > 10^{3.5} \text{ cm}^{-3}$ ) as opposed to strictly dense gas above  $n > 10^{4.5} \text{ cm}^{-3}$ . This result appears in agreement with more recent studies of HCN emission in Milky Way clouds that find HCN emission

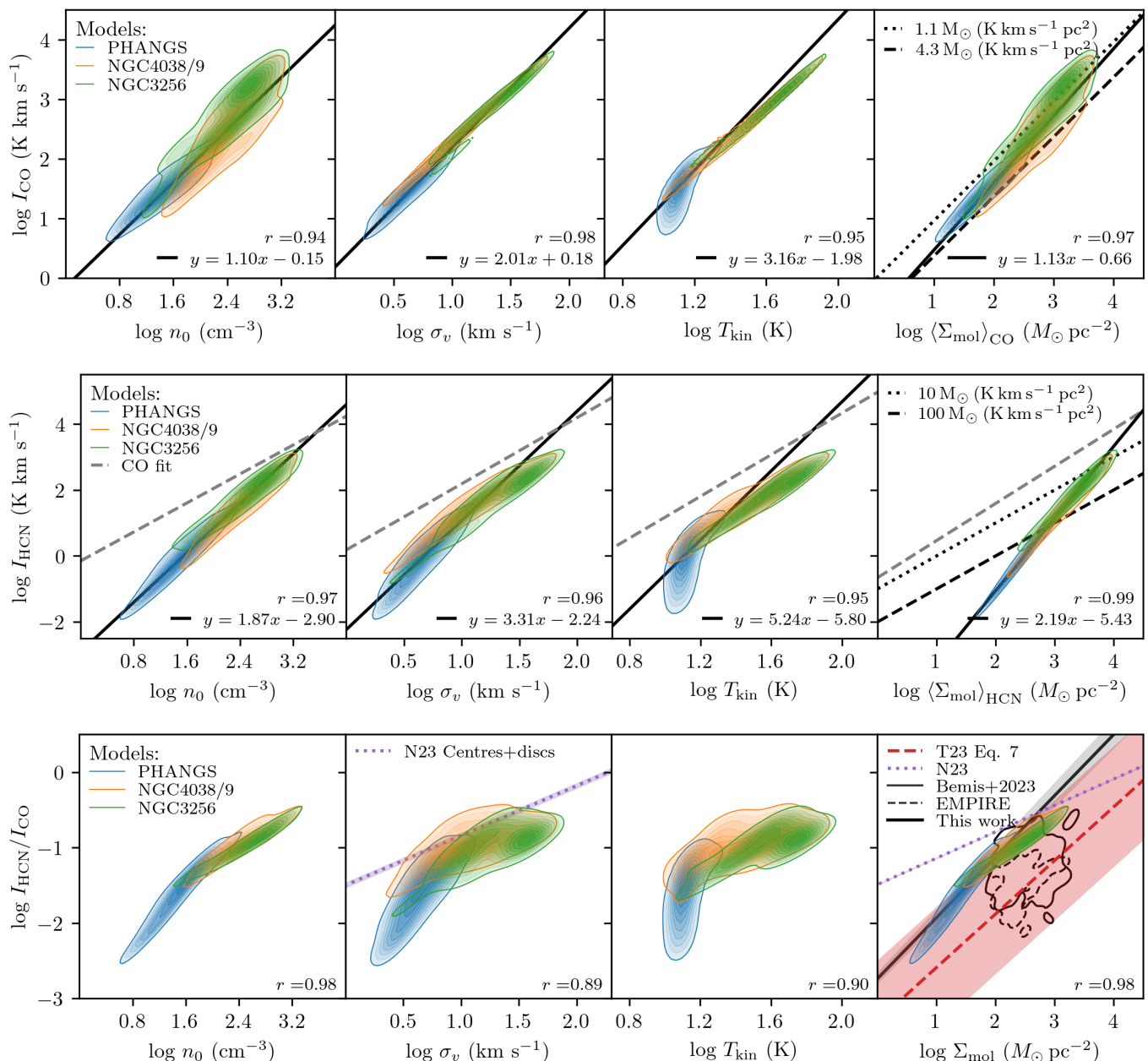


**Fig. 5.** The CO intensity (top row), the HCN intensity (center row), and HCN/CO ratio (bottom row) as a function of mean gas density, velocity dispersion, kinetic temperature, and gas column density. The column densities shown are from Eq. 12 for  $I_{\text{CO}}$  and  $I_{\text{HCN}}$  (top and center rows) and are the fiducial model column densities for the HCN/CO ratio (bottom row). Reference conversion factor values are shown in the intensity vs. column density plots as the dotted and dashed lines. We show the CO fits (top row) in the HCN plots (center row) as the gray dashed lines. Spearman rank coefficients are shown in the lower right corner. Formatting is the same as in Fig. 3. We plot fits from the results of the ALMOND survey (purple, dotted line Neumann et al. 2023) and Tafalla et al. (2023) (red, dashed line). Uncertainties on their respective fits are shown as the shaded areas. For comparison, we plot the results of Paper I sample (solid contours) and the EMPIRE sample (dashed contours, Jiménez-Donaire et al. 2019) in the HCN/CO ratio vs. gas surface density plot. Our models show strong, positive correlations between the modelled line intensities and mean density, velocity dispersion, mean kinetic temperature, and gas column densities.  $I_{\text{HCN}}$  appears to increase more rapidly with each of these parameters compared to  $I_{\text{CO}}$ . Spearman rank coefficients are shown in the lower right corner of each plot.

includes more moderate gas densities, e.g.  $n \sim 800 \text{ cm}^{-3}$  (e.g. Kauffmann et al. 2017). Our models include a range of cloud properties, including those found in normal galaxies (i.e. PHANGS models) as well as more extreme cloud models based on cloud properties from the Antennae and NGC3256. We find evidence that  $I_{\text{HCN}}/I_{\text{CO}}$  tracks a gas fraction including more moderate gas densities even in the more extreme environments.

### 3.3. Using estimates of CO and HCN Emissivity to Derive Gas Masses

We explore if the dense gas fraction can be consistently recovered from observations of HCN and CO using luminosity-to-mass conversion factors, which are commonly used to estimate molecular gas masses from molecular line observations. We recall from section 2.4.1 that emissivity can be recast in units of luminosity-to-mass conversion factors, such that  $\alpha_{\text{mol}} \propto$

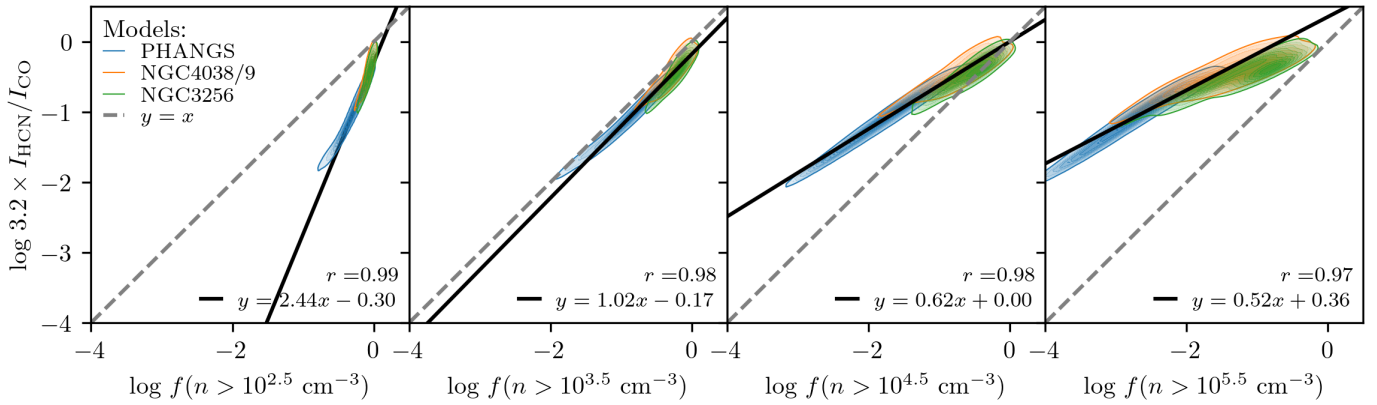


**Fig. 6.**  $3.2 \times I_{\text{HCN}}/I_{\text{CO}}$  as a function of the fraction of gas above (from left to right)  $n \sim 10^{2.5}$ ,  $10^{3.5}$ ,  $10^{4.5}$  and  $10^{5.5} \text{ cm}^{-3}$ . Formatting is the same as in Fig. 3. Fits are shown as the solid black line and listed in the legend. The modelled  $I_{\text{HCN}}/I_{\text{CO}}$  scales most directly (has a slope closest to unity) with  $f(n > 10^{3.5} \text{ cm}^{-3})$ , supporting previous findings that this line ratio is sensitive to gas above moderate densities. Although not shown here, the same is found when comparing the emissivity ratio,  $\langle \epsilon_{\text{HCN}} \rangle / \langle \epsilon_{\text{CO}} \rangle$ , with the same gas fractions. Spearman rank coefficients are shown in the lower right corner of each plot.

$1/\langle \epsilon_{\text{mol}} \rangle$ , with the caveat that emissivities derived in this work are relative to true cloud surface densities, rather than integrated quantities such as mass and molecular line luminosity. By construction, the ratio of our modelled intensities will be proportional to the ratio of molecular line luminosities analogous to those measured in resolved or unresolved observations, or the ratio of line intensities of resolved observations. We note that for the remainder of this work, we use  $\langle \alpha_{\text{mol}} \rangle$  when we are referring to the inverse of modelled emissivity of a molecular transition, and  $\alpha_{\text{mol}}$  when referring to an estimate of the idealised mass conversion factor of a molecular transition (which may also include additional factors, such as filling fraction).

In Fig. 7, we present the CO and HCN emissivities from our models, and contrast these against idealised luminosity-to-mass conversion factors. We fit the relationship between  $\langle \alpha_{\text{CO}} \rangle = 1/\langle \epsilon_{\text{CO}} \rangle$  and  $I_{\text{CO}}$  using orthogonal distance regression and find:

$$\log \left( \frac{\alpha_{\text{CO}}}{M_{\odot} (\text{K km s}^{-1} \text{ pc}^2)^{-1}} \right) = (-0.26_{-0.04}^{0.03}) \log \left( \frac{I_{\text{CO}}}{\text{K km s}^{-1}} \right) \quad (17)$$

$$+ 0.90 \pm 0.07. \quad (18)$$

Uncertainties are determined using bootstrapping. We show in Fig. 7 that our CO emissivities agree well with the Narayanan et al. (2012) prescription for the CO-to- $\text{H}_2$  conversion factor. We find a similar slope, -0.26, compared to -0.32 in (Narayanan et al. 2012). We also compare with the numerical works of Hu et al. (2022a) and Gong et al. (2020). The prescription taken from Hu et al. (2022a), in particular, is for 1 kpc scales, which might explain the offset between their prescription and ours, but has roughly a similar slope (-0.43). In their work they also include modelling of  $\alpha_{\text{CO}}$  at higher resolution and do find higher values more consistent with our modelling. The Gong et al. (2020) relationship has a shallower slope than our trend, which appears inconsistent with some of the most recent studies of  $\alpha_{\text{CO}}$  in nearby galaxies (e.g. He et al. 2024; Teng et al. 2024). We also compare with observationally-derived estimates of  $\alpha_{\text{CO}}$  at  $\sim 150 \text{ pc}$  scales in the Antennae (He et al. 2024) and PHANGS galaxies (Teng et al. 2024). We find good agreement with these studies. We note that we have recast the  $\alpha_{\text{CO}} - \sigma_v$  fit from Teng et al. (2024) in terms of  $I_{\text{CO}}$  using the fit between  $I_{\text{CO}}$  and  $\sigma_v$  from our models. Additionally, we find that there is little difference between  $1/\langle \epsilon_{\text{CO}} \rangle$  and our model estimates of  $\alpha_{\text{CO}}$ , where we divide the

model column density by  $I_{\text{CO}}$  directly. This agreement is a reflection of how well the column of mass traced by CO  $J = 1 - 0$  tracks the mean  $\text{H}_2$  column density of our models, and further reinforces the utility of CO  $J = 1 - 0$  as a tracer of the total molecular gas content in molecular clouds in nearby galaxies. On average,  $\alpha_{\text{CO}}$  decreases with increasing  $I_{\text{CO}}$  which is a reflection of increasing CO excitation as well as variations in CO optical depth. Overall, our model estimates of  $\langle \alpha_{\text{CO}} \rangle = 1/\langle \epsilon_{\text{CO}} \rangle$  appear to agree well with prescriptions from numerical work (e.g. Narayanan et al. 2012) as well as recent, high-resolution studies of molecular gas in galaxies we have used as our model templates (e.g. He et al. 2024; Teng et al. 2024).

We see a similar decrease in  $1/\langle \epsilon_{\text{HCN}} \rangle$  with increasing  $I_{\text{HCN}}$ , but find that values of  $1/\langle \epsilon_{\text{HCN}} \rangle$  span over  $\sim 2.5$  dex, while values of  $1/\langle \epsilon_{\text{CO}} \rangle$  span  $\sim 1$  dex in our models. We fit the relationship between  $\langle \alpha_{\text{HCN}} \rangle = 1/\langle \epsilon_{\text{HCN}} \rangle$  and  $I_{\text{HCN}}$  using orthogonal distance regression and find:

$$\log \left( \frac{\alpha_{\text{HCN}}}{M_{\odot} (\text{K km s}^{-1} \text{ pc}^2)^{-1}} \right) = (-0.55 \pm 0.01) \log \left( \frac{I_{\text{HCN}}}{\text{K km s}^{-1}} \right) \quad (19)$$

$$+ 2.55 \pm 0.01. \quad (20)$$

Again, uncertainties are determined using bootstrapping. We also see in Fig. 7 that the Gao & Solomon (2004a,b) value for  $\alpha_{\text{HCN}}$  is only consistent with the brightest  $I_{\text{HCN}}$  in our models. Several recent studies of Milky Way clouds find evidence of larger values of  $\alpha_{\text{HCN}}$  relative to the original estimate by Gao & Solomon (2004a,b). An estimate of  $\alpha_{\text{HCN}} = 92 (M_{\odot} [\text{K km s}^{-1} \text{ pc}^2]^{-1})$  in the Perseus Molecular Cloud from Dame & Lada (2023) falls within the range of  $1/\langle \epsilon_{\text{HCN}} \rangle$  found in our models. They derive  $\alpha_{\text{HCN}}$  by comparing observations of HCN  $J = 1 - 0$  luminosity with gas mass estimates derived from extinction measurements of dust. Dame & Lada (2023) also note that HCN brightness has a significant effect on the value of  $\alpha_{\text{HCN}}$ , and when the original Gao & Solomon (2004a,b) value is scaled by an HCN brightness temperature more appropriate for Galactic GMCs they derive a value more consistent with their measurement from Perseus. We also compare with the results of Shima et al. (2017) in Fig. 7, and find good agreement with the values they derive for Aquila, Ophiuchus, and Orion B. Tafalla et al. (2023) also derive estimates of  $\alpha_{\text{HCN}}$  in Milky Way clouds using extinction estimates. They



find  $\alpha_{\text{HCN}} = 23, 46, \text{ and } 73 M_{\odot} (\text{K km s}^{-1} \text{pc}^2)^{-1}$  for the California, Orion A, and Perseus molecular clouds, respectively. Additionally, [Forbrich et al. \(2023\)](#) find evidence of deviations in  $\alpha_{\text{HCN}}$  from the original estimate of [Gao & Solomon \(2004a,b\)](#). They find  $\alpha_{\text{HCN}} \approx 1 (M_{\odot} [\text{K km s}^{-1} \text{pc}^2])^{-1}$  in six GMCs in Andromeda by comparing estimates of dust with HCN emission. When assuming the Milky way dust-to-gas mass ratio, they find a much larger value of  $\alpha_{\text{HCN}} \approx 109 (M_{\odot} [\text{K km s}^{-1} \text{pc}^2])^{-1}$ , similar to that of [Dame & Lada \(2023\)](#). We note that the [Tafalla et al. \(2023\)](#) estimate for Perseus is slightly lower than that quoted by [Dame & Lada \(2023\)](#), which they argue is potentially from extended HCN emission not included in the mapping area of the [Dame & Lada \(2023\)](#) study. However, we find the opposite effect on  $\alpha_{\text{HCN}}$  ( $1/\langle\epsilon_{\text{HCN}}\rangle$ ) when we exclude HCN emission from lower column densities in our models (cf. Appendix C) and conclude that this discrepancy could, in part, be due to the sensitivity limit of the [Tafalla et al. \(2023\)](#) study.

Despite the broader range in HCN emissivity relative to CO emissivity, we find that  $I_{\text{HCN}}/I_{\text{CO}}$  closely tracks the fraction of gas above  $n > 10^{3.5} \text{ cm}^{-3}$ , which implies a nearly constant HCN and CO luminosity-to-mass ratio,  $\alpha_{\text{HCN}}/\alpha_{\text{CO}}$ , can be used to estimate  $f(n > 10^{3.5} \text{ cm}^{-3})$  from observations (cf. Fig. 8). Regardless of the absolute value of  $\alpha_{\text{HCN}}/\alpha_{\text{CO}}$ , the results of our modelling suggest that the fraction of gas above  $n > 10^{3.5} \text{ cm}^{-3}$  can be roughly estimated by applying a fixed  $\alpha_{\text{HCN}}/\alpha_{\text{CO}}$  ratio to  $I_{\text{HCN}}/I_{\text{CO}}$ , although this ratio appears to be larger than our initially assumed value of  $\alpha_{\text{HCN}}/\alpha_{\text{CO}} = 3.2$ . These results suggest that (1) the HCN intensity scales with the fraction of mass above moderate gas densities, and (2) a constant ratio between  $\alpha_{\text{HCN}}/\alpha_{\text{CO}}$  can be assumed to derive this fraction of gas using  $I_{\text{HCN}}/I_{\text{CO}}$ . Furthermore, our models predict that  $\alpha_{\text{HCN}}$  does not scale directly with the emissivity of HCN. This difference in behaviour between  $1/\langle\epsilon_{\text{HCN}}\rangle$  and  $\alpha_{\text{HCN}}$  in our models is a reflection of HCN  $J = 1 - 0$  being primarily subthermally excited.

We reframe the results above in terms of the ratio of the HCN and CO luminosity-to-mass conversion factors,  $\alpha_{\text{HCN}}/\alpha_{\text{CO}}$  by multiplying the ratio of  $I_{\text{HCN}}/I_{\text{CO}}$  by the fraction of mass with densities above  $n_{\text{thresh}} > 10^{3.5} \text{ cm}^{-3}$  and  $n_{\text{thresh}} > 10^{4.5} \text{ cm}^{-3}$ , e.g.:

$$f(n > n_{\text{thresh}}) = \frac{\alpha_{\text{HCN}}}{\alpha_{\text{CO}}} \times \frac{I_{\text{HCN}}}{I_{\text{CO}}}. \quad (21)$$

Thus, when the ratio of  $\alpha_{\text{HCN}}/\alpha_{\text{CO}}$  is multiplied with  $I_{\text{HCN}}/I_{\text{CO}}$ , we get an estimate of said gas mass fraction, i.e.:

$$f(n > n_{\text{thresh}}) = \frac{M_{\text{H}_2}(n > n_{\text{thresh}})}{M_{\text{H}_2, \text{tot}}}. \quad (22)$$

We show these results in Fig. 8 as a function of  $I_{\text{HCN}}/I_{\text{CO}}$ . We find that  $\alpha_{\text{HCN}}/\alpha_{\text{CO}}$  is relatively constant when assuming  $I_{\text{HCN}}$  tracks the mass above  $n > 10^{3.5} \text{ cm}^{-3}$ . To derive the fraction of gas above  $n > 10^{3.5} \text{ cm}^{-3}$ , our models predict that one can apply  $\alpha_{\text{HCN}}/\alpha_{\text{CO}} \approx 5$  to  $I_{\text{HCN}}/I_{\text{CO}}$ . Contrary to this,  $\alpha_{\text{HCN}}/\alpha_{\text{CO}}$  must increase with  $I_{\text{HCN}}/I_{\text{CO}}$  when assuming  $I_{\text{HCN}}$  tracks the mass above  $n > 10^{4.5} \text{ cm}^{-3}$ . Although not shown in Fig. 8, this relationship is even steeper when considering  $f(n > 10^{5.5} \text{ cm}^{-3})$ . This analysis is consistent with our findings in Fig. 6, where we see that  $I_{\text{HCN}}/I_{\text{CO}}$  scales most directly (linearly) with the fraction of gas above  $n > 10^{3.5} \text{ cm}^{-3}$ .

These results suggest that, in theory, the fraction of dense gas above  $n > 10^{4.5} \text{ cm}^{-3}$  can be derived from  $I_{\text{HCN}}/I_{\text{CO}}$  if one adopts a prescription for  $\alpha_{\text{HCN}}/\alpha_{\text{CO}}$  that increases with  $I_{\text{HCN}}/I_{\text{CO}}$ . However, our models show that estimates of dense gas mass using the original estimate of  $\alpha_{\text{HCN}}$  from [Gao & Solomon \(2004a,b\)](#)

likely *overestimate* the true dense gas mass, except in the most extreme cases like galaxy mergers and U/LIRGs. This overestimate is more significant for disk galaxies, such as the Milky Way and galaxies in the PHANGS sample. It may be more useful to observe other molecular line transitions that are exclusively sensitive to higher gas densities, such as  $\text{N}_2\text{H}^+$  ([Kauffmann et al. 2017](#); [Pety et al. 2017](#); [Priestley et al. 2023](#)) to estimate  $f(n > 10^{4.5} \text{ cm}^{-3})$ , rather than attempting to calibrate the relationship between  $I_{\text{HCN}}/I_{\text{CO}}$  and  $f(n > 10^{4.5} \text{ cm}^{-3})$ .

Despite HCN having a higher critical density than  $\text{N}_2\text{H}^+$ ,  $\text{N}_2\text{H}^+$  appears to more reliably trace cool, dense gas in Milky Way molecular clouds ([Kauffmann et al. 2017](#); [Pety et al. 2017](#); [Tafalla et al. 2021](#)), whereas HCN emission tends to originate from gas at more moderate temperatures ([Pety et al. 2017](#); [Barnes et al. 2020](#)) and more moderate gas densities ([Kauffmann et al. 2017](#); [Pety et al. 2017](#)). There are several chemical processes that limit  $\text{N}_2\text{H}^+$  emission to regions of primarily dense, cool gas ( $T < 20 \text{ K}$ ).  $\text{N}_2\text{H}^+$  is destroyed in the presence of CO via ion-neutral interactions ([Meier & Turner 2005](#)). Furthermore, the creation of  $\text{N}_2\text{H}^+$  depends on the availability of  $\text{H}_3^+$  to react with  $\text{N}_2$ , which is a chemical process in competition with the creation of CO. Thus,  $\text{N}_2\text{H}^+$  is primarily abundant in regions where CO is depleted onto dust grains ([Caselli & Ceccarelli 2012](#)), unlike HCN which is present also at moderate densities of gas overlapping with CO ([Kauffmann et al. 2017](#); [Pety et al. 2017](#)). Thus,  $\text{N}_2\text{H}^+$  may be a better tracer of the cold, dense gas that serves as the direct fuel for star formation.

Interestingly, [Jiménez-Donaire et al. \(2023\)](#) find that  $\text{N}_2\text{H}^+$  and HCN have a nearly constant ratio over a large range of spatial scales. They compare observations of  $\text{N}_2\text{H}^+$  and HCN in NGC 6946 at 1 kpc scales with existing literature values of other galaxies ([Mauersberger & Henkel 1991](#); [Nguyen et al. 1992](#); [Watanabe et al. 2014](#); [Aladro et al. 2015](#); [Nishimura et al. 2016](#); [Takano et al. 2019](#); [Eibensteiner et al. 2022](#)) and Milky Way clouds ([Jones et al. 2012](#); [Pety et al. 2017](#); [Barnes et al. 2020](#); [Yun et al. 2021](#)), and find this ratio is  $I_{\text{N}_2\text{H}^+}/I_{\text{HCN}} = 0.15 \pm 0.02$  averaged over parsec-scales and kpc-scales. Due to the segregation of  $\text{N}_2\text{H}^+$  in CO-depleted regions of molecular clouds, [Jiménez-Donaire et al. \(2023\)](#) conclude that the linear scaling between HCN and  $\text{N}_2\text{H}^+$  must be a product of the self-similarity of clouds, and that HCN emission may still be a valuable dense gas tracer to assess the properties of the cooler, denser  $\text{N}_2\text{H}^+$ -emitting gas. However, extragalactic observations of  $\text{N}_2\text{H}^+$  are so far limited to a handful of nearby galaxies, and have yet to be completed at cloud-scales. Thus, it remains an important next step to perform comparable observations of  $\text{N}_2\text{H}^+$  and HCN over a large sample of cloud environments in nearby galaxies.

### 3.4. $I_{\text{HCN}}/I_{\text{CO}}$ and the fraction of gravitationally-bound gas

We explore how well the  $I_{\text{HCN}}/I_{\text{CO}}$  ratio tracks gravitationally-bound fraction of gas ( $f_{\text{grav}}$ ) as predicted by the LN+PL analytical models of star formation. We emphasize here that we are interested in general trends that are predicted by turbulent models of star formation, and the LN+PL analytical models of star formation ([Burkhart 2018](#)) agree closely with those of the LN-only models ([Krumholz & McKee 2005](#); [Padoan & Nordlund 2011](#)). As such, we only compare against the results of the LN+PL analytical models of star formation.

In Fig. 9, we plot the modelled  $I_{\text{HCN}}/I_{\text{CO}}$  ratio and dense gas fraction,  $f(n > 10^{4.5} \text{ cm}^{-3})$  against  $f_{\text{grav}}$ . We take  $f_{\text{grav}}$  to be the fraction of gas in the powerlaw component of the LN+PL model (see Equation 20 in [Burkhart & Mocz 2019](#)). We find that  $I_{\text{HCN}}/I_{\text{CO}}$  has a strong, negative correlation with  $f_{\text{grav}}$ . This is

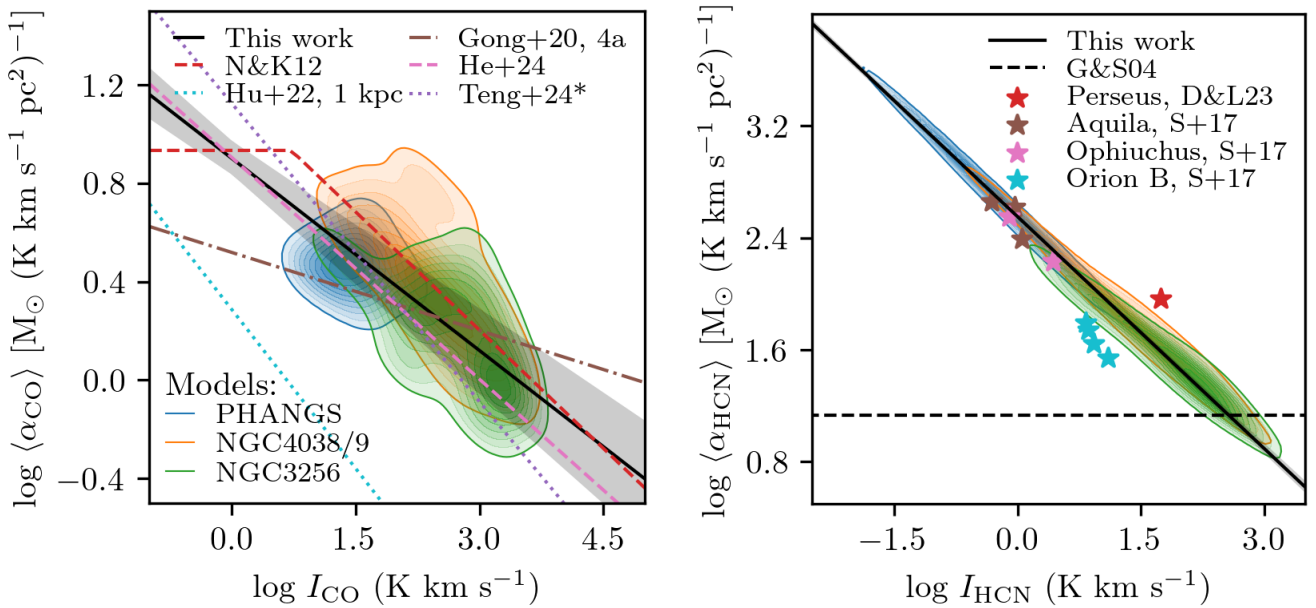


**Fig. 7.** *Left:* The inverse of the CO emissivity (in units of the CO conversion factor) as a function of CO intensity,  $\langle \alpha_{\text{CO}} \rangle = \langle \epsilon_{\text{CO}} \rangle^{-1}$ . We include the fit to our models (Eq. 17, solid line) and the one sigma uncertainty on the fit (gray shaded area). We also include the results of several numerical studies (Narayanan et al. 2012; Hu et al. 2022a; Gong et al. 2020, the red dashed line, cyan dotted line, and brown dash-dotted line, respectively) as well as the results of observational studies at  $\sim 150$  pc-scales in the Antennae (pink dashed line, He et al. 2024) and PHANGS galaxies (purple dotted line, Teng et al. 2024). \*We note that we have recast the  $\alpha_{\text{CO}} - \sigma_v$  fit from Teng et al. (2024) in terms of  $I_{\text{CO}}$  and  $\sigma_v$  from our models. *Right:* The inverse of the HCN emissivity (in units of the HCN conversion factor) as a function of HCN intensity,  $\langle \alpha_{\text{HCN}} \rangle = \langle \epsilon_{\text{HCN}} \rangle^{-1}$ . We include a fit to our models (Eq. 19, solid line) and the one sigma uncertainty on the fit (gray shaded area). For comparison, we include several published values of  $\alpha_{\text{HCN}}$  from observations of Milky Way clouds (Dame & Lada 2023; Shimajiri et al. 2017), and we show the Gao & Solomon (2004a,b) value as the black, solid horizontal line. This figure demonstrates how well our models are able to reproduce previous numerical prescriptions of  $\alpha_{\text{CO}}$ , as well observationally-constrained values of  $\alpha_{\text{CO}}$  and  $\alpha_{\text{HCN}}$ . Formatting of the model output is the same as in Fig. 3.

consistent with the results of Paper I, where we made a similar conclusion without including radiative transfer in our analysis.  $f(n > 10^{4.5} \text{ cm}^{-3})$  has an even steeper, negative correlation with  $f_{\text{grav}}$ . We note that the primary driver of the decrease in  $f_{\text{grav}}$  towards higher  $I_{\text{HCN}}/I_{\text{CO}}$  and  $f(n > 10^{4.5} \text{ cm}^{-3})$  is a reflection of the higher gas velocity dispersion in these models (which correspond to models with higher gas surface density and wider  $n - \text{PDFs}$ ). We also find that models with the lowest estimates of  $f_{\text{grav}}$  and highest  $f(n > 10^{4.5} \text{ cm}^{-3})$  have the *shortest* depletion times, and the corresponding modelled  $I_{\text{HCN}}/I_{\text{CO}}$  and predicted depletion times are consistent with our data (cf. Fig 9). In general, the models of star formation we consider predict that turbulence acts as a process to the gas that prevents gravitational collapse of gas. Indeed, we find that the transition density (the density at which gas becomes self-gravitating in our models) increases across our model parameter space from  $n = 10^{4.5} \text{ cm}^{-3}$  in the PHANGS-type models to  $n = 10^{5.9} \text{ cm}^{-3}$  and  $n = 10^{6.6} \text{ cm}^{-3}$  in the NGC4038/9- and NGC3256-type models, respectively. We also note that the transition density for the PHANGS-type models agrees well with the estimation for the threshold density for star formation in the Milky Way (e.g.  $n \gtrsim 10^4 \text{ cm}^{-3}$ , Lada et al. 2010, 2012).

We also show in Fig. 9 that models with higher  $I_{\text{HCN}}/I_{\text{CO}}$  and lower  $f_{\text{grav}}$  are, on average, still consistent with observations and have overall shorter total gas depletion times ( $t_{\text{dep}}$ ), as is also seen in observations and is in agreement with the results of Paper I. The above results also have important implications for the interpretation of dense gas depletion times. These results support that the longer  $t_{\text{dep,dense}}$  observed towards higher  $I_{\text{HCN}}/I_{\text{CO}}$  in our data (assuming fixed  $\alpha_{\text{HCN}}/\alpha_{\text{CO}}$ ) do not necessarily imply lower star

formation efficiencies of the directly star-forming gas, but rather that a smaller fraction of the dense gas is unstable to collapse in these systems (see right panel of Fig 9). We confirm that  $f_{\text{grav}}$  is predicted to decrease from 1.7% in the PHANGS-type models to 0.8% and 0.6% in the NGC4038/9- and NGC3256-type models, respectively. In contrast to this, the fraction of *dense* gas above  $n = 10^{4.5} \text{ cm}^{-3}$  increases from 1.9% in the PHANGS-type models to 22% and 30% in the NGC4038/9- and NGC3256-type models, respectively. It is also interesting to note that in the PHANGS-type models  $f_{\text{grav}}$  is well-matched to  $f_{\text{dense}}$ .

### 3.5. The Impact of CO and HCN Emissivity on Star Formation Relations

We consider here how variations in emissivity can impact the scatter as well as the general trends of some star formation relations. One of the differences between the results shown in Paper I and this work is the origin of the scatter in the various star formation scaling relationships. In Paper I, the scatter produced in the modeled star formation scaling relationships is partially from changes in  $\epsilon_{\text{ff}}$  due to variations in PL slope for the LN+PL models or variations in turbulence (quantified by the sonic Mach number) for the LN-only models. In this work, we also show that variations in the emissivity of CO contribute to and may even account for the majority of the scatter in observational star formation scaling relationships.

For example, we show in Fig. 10 that the modelled trend in  $\epsilon_{\text{ff}}$  with  $P_{\text{turb}}$  agrees well with observations under the assumption of a fixed  $\alpha_{\text{CO}}$  and assuming mean density scales with gas surface density. We plot  $\epsilon_{\text{ff}}$  versus  $P_{\text{turb}}$  using method 1 described

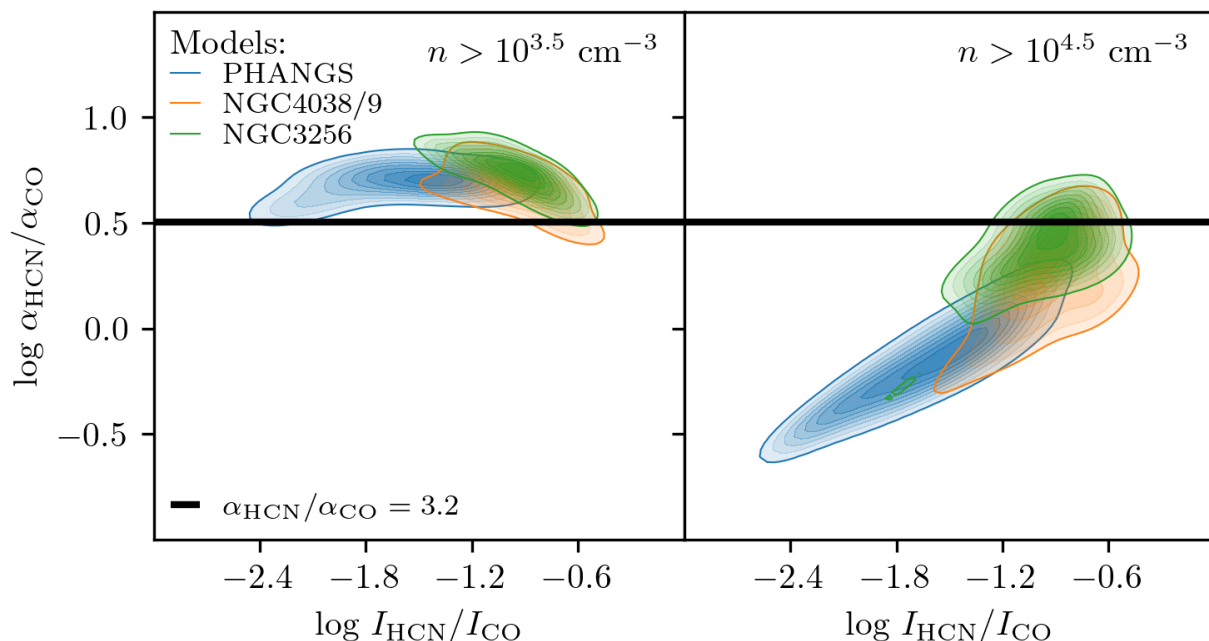


**Fig. 8.** The ratio of the HCN and CO conversion factors (given in Eq. 21) as a function of the ratio of the HCN and CO intensities, where we consider  $\alpha_{\text{HCN}}$  as conversion factor for the total mass above  $n > 10^{3.5} \text{ cm}^{-3}$  (left) and  $n > 10^{4.5} \text{ cm}^{-3}$  (right). For comparison, we plot  $\alpha_{\text{HCN}}/\alpha_{\text{CO}} = 3.2$  (solid, black line), which is the ratio of the Gao & Solomon (2004a,b) conversion factor and Milky Way CO conversion factor. Formatting is the same as in Fig. 3. This figure demonstrates how emissivity is sensitive to the intensity per mass traced by a particular transition, whereas luminosity-to-mass conversion factors account for additional factors that allow us to estimate specific masses, e.g. total gas mass and dense gas mass, that may not be fully reflected in the molecular emissivity. We find that due to the subthermal excitation of HCN  $J = 1 - 0$ , this transition is a poor tracer of the of the gas mass above  $n > 10^{4.5} \text{ cm}^{-3}$  and is a better tracer of moderate gas densities ( $n > 10^{3.5} \text{ cm}^{-3}$ ), as found in previous observational studies.

at the beginning of the results section, which is analogous to the method used to derive gas surface densities from observations. For comparison, we also plot  $t_{\text{dep}}$  as a function of the HCN/CO ratio in Fig. 10. In these two plots the scatter in our models primarily comes from variations in CO intensity (since we have fixed PL slope). The scatter is also correlated with variations in CO emissivity. This is apparent in the gradient in  $\langle \alpha_{\text{CO}} \rangle = 1/\langle \epsilon_{\text{CO}} \rangle$  across the color points in the left two panels of Fig. 10. Models with lower CO intensity (which in general have higher  $\alpha_{\text{CO}}$  and lower CO emissivity, see Fig. 7) appear to have higher  $\epsilon_{\text{ff}}$  and vice versa (Fig. 10). This agrees with the trend we observe in our data in Bemis & Wilson (2023) (also shown in Fig. 10) where we have adopted a fixed CO conversion factor and assumed mean gas density scales with gas surface density. These results show that variations in CO emissivity can account for a significant amount of scatter observed in star formation scaling relations. When we apply  $\langle \alpha_{\text{CO}} \rangle = 1/\langle \epsilon_{\text{CO}} \rangle$  to our modelled  $I_{\text{CO}}$  to estimate gas surface density (while still using the assumption that the mean gas volume density scales with with gas surface density), we produce tighter trends in  $\epsilon_{\text{ff}}$  with  $P_{\text{turb}}$  and  $t_{\text{dep}}$  with HCN/CO (purple lines) that are qualitatively more consistent with the actual model predictions (red lines, left two panels of Fig. 10). The offset in  $\epsilon_{\text{ff}}$  and  $t_{\text{dep}}$  between the model prediction and what is obtained when we apply  $\langle \alpha_{\text{CO}} \rangle = 1/\langle \epsilon_{\text{CO}} \rangle$  to our modelled  $I_{\text{CO}}$  in Fig. 10 is a result of modelled CO emission missing a fraction of the lower surface density gas in our models, analogous to “CO-dark” gas (cf. Bolatto et al. 2013). When we scale  $\langle \epsilon_{\text{CO}} \rangle^{-1}$  by the ratio between the true model gas surface density and  $\langle N_{\text{CO}} \rangle$  we find nearly identical trends.

We quantify the scatter in  $\epsilon_{\text{ff}}$  vs.  $P_{\text{turb}}$  by fitting a line to the relationship and calculating the standard deviation on the

$y$ -residuals. Assuming constant conversion factors, the scatter in the  $\epsilon_{\text{ff}}$  vs.  $P_{\text{turb}}$  relationship is  $\sim 0.36$  using method 1 and becomes  $\sim 0.05$  when we apply  $\langle \alpha_{\text{CO}} \rangle = 1/\langle \epsilon_{\text{CO}} \rangle$ , which is similar to the scatter in the theoretical prediction ( $\sim 0.02$ ). The scatter in  $t_{\text{dep}}$  with HCN/CO is  $\sim 0.21$  when assuming constant conversion factors and becomes  $\sim 0.12$  when we apply  $\langle \alpha_{\text{CO}} \rangle = 1/\langle \epsilon_{\text{CO}} \rangle$ . The scatter in the theoretical prediction is  $\sim 0.18$ . We conclude that a significant portion of the scatter in these relationships originates from variations in emissivity in our models.

We calculate Spearman rank coefficients between  $\langle \alpha_{\text{CO}} \rangle = 1/\langle \epsilon_{\text{CO}} \rangle$  and  $\langle \tau_{\text{CO}} \rangle$ ,  $\langle T_{\text{ex,CO}} \rangle$ ,  $\sigma_v$ ,  $\Sigma_{\text{mol}}$ ,  $n_0$ ,  $T_{\text{kin}}$ , and  $\langle I_{\text{CO}} \rangle$  to assess the strength of the correlation between these parameters. We find that  $\langle \alpha_{\text{CO}} \rangle$  only strongly ( $|r| > 0.7$ ) correlates with  $\langle \tau_{\text{CO}} \rangle$  ( $r = 0.9$ ) in our models.  $\langle \alpha_{\text{CO}} \rangle$  is moderately ( $0.5 < |r| < 0.7$ ) correlated with  $\sigma_v$  ( $r = -0.6$ ) and  $\langle I_{\text{CO}} \rangle$  ( $r = -0.5$ ).  $\alpha_{\text{CO}}$  is weakly ( $|r| < 0.5$ ) correlated with the remainder of the parameters ( $\langle T_{\text{ex,CO}} \rangle$ ,  $\Sigma$ ,  $n_0$ , and  $T_{\text{kin}}$ ). This suggests that variations in CO emissivity are primarily driven by changes in optical depth in our models. Furthermore, the connection between  $\langle \alpha_{\text{CO}} \rangle$  and  $\langle \tau_{\text{CO}} \rangle$  likely stems from variations in gas velocity dispersion, since higher gas velocity dispersions are connected to lower optical depths in our models and higher CO intensities, as shown in Fig. 4. This also explains the variations we see in  $\langle \alpha_{\text{CO}} \rangle$  in the scatter of e.g.  $\epsilon_{\text{ff}}$  with  $P_{\text{turb}}$  and  $t_{\text{dep}}$  with HCN/CO, since the scatter of our model parameter space (shown in Fig. 2) is set by variations in velocity dispersion. We can also conclude that variations in  $\langle \alpha_{\text{CO}} \rangle$  are, to a lesser effect, driven by variations in the mean gas density that the CO emission originates from, but  $\langle \alpha_{\text{CO}} \rangle$  is more strongly correlated with  $T_{\text{kin}}$  ( $r = -0.4$ ) relative to  $n_0$  ( $r = -0.2$ ) in our models. We note that CO emissivity is also impacted by the width of the  $n - \text{PDF}$ , which is set by



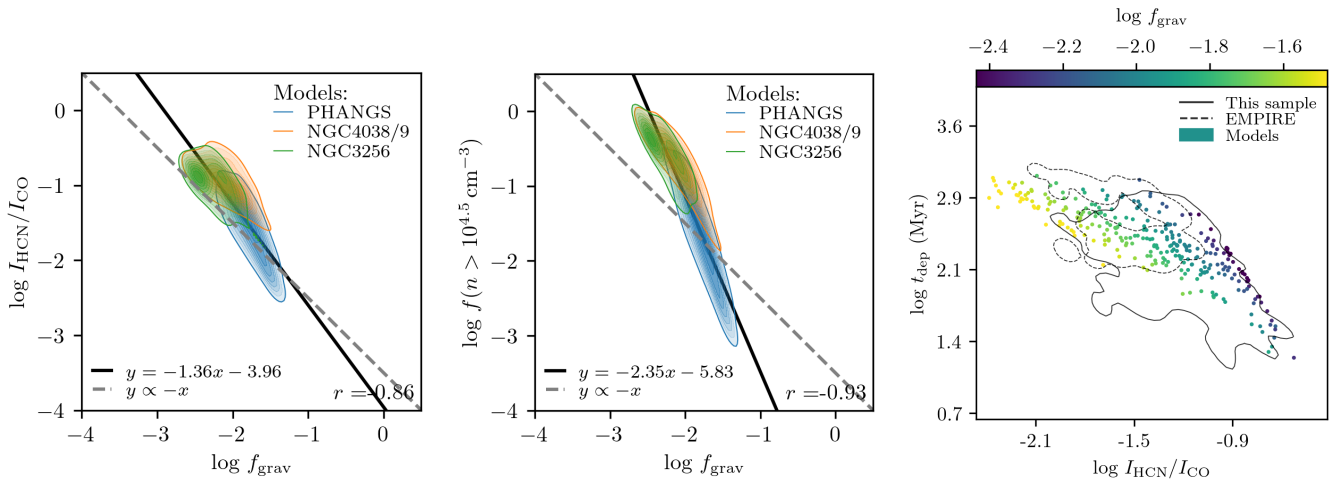


**Fig. 9.** *Left:* Modelled  $I_{\text{HCN}}/I_{\text{CO}}$  as a function of the gravitationally-bound fraction of gas ( $f_{\text{grav}}$ ) predicted by the LN+PL analytical models of star formation. *Center:* The fraction of dense gas above  $n > 10^{4.5} \text{ cm}^{-3}$  as a function of the gravitationally-bound fraction of gas ( $f_{\text{grav}}$ ) predicted by the LN+PL analytical models of star formation. Formatting is the same as in Fig. 3. Spearman rank coefficients are shown in the lower right corner of the left and center panels. *Right:* Total gas depletion time ( $t_{\text{dep}}$ ) as a function of  $I_{\text{HCN}}/I_{\text{CO}}$  ratio. Models are shown as the color points. Measurements of  $t_{\text{dep}}$  and  $I_{\text{HCN}}/I_{\text{CO}}$  from our sample of galaxies and the EMPIRE sample are shown as the solid black and dashed black contours, respectively. Our models find that the  $I_{\text{HCN}}/I_{\text{CO}}$  ratio is negatively correlated with  $f_{\text{grav}}$  as predicted by gravoturbulent models of star formation. Additionally, the fraction of dense gas above  $n > 10^{4.5} \text{ cm}^{-3}$  has an even steeper, negative correlation with  $f_{\text{grav}}$  as predicted by gravoturbulent models of star formation (e.g. Burkhardt 2018; Burkhardt & Mocz 2019). Thus, although  $I_{\text{HCN}}/I_{\text{CO}}$  is sensitive to gas above moderate densities, we conclude that a single molecular line ratio, such as HCN/CO, does not necessarily scale with the fraction of directly star-forming gas in clouds. We also find that models with the lowest estimates of  $f_{\text{grav}}$  and highest  $f(n > 10^{4.5} \text{ cm}^{-3})$  have the *shortest* depletion times, and the corresponding modelled  $I_{\text{HCN}}/I_{\text{CO}}$  and predicted depletion times are consistent with our data.

a combination of the turbulent velocity dispersion and gas kinetic temperature in our models. Thus, inconsistencies between observationally-derived quantities and model predictions, such as  $\epsilon_{\text{ff}}$ , may in part be due to uncertainties in mean gas density, but are also likely driven by a number of other quantities (i.e. gas velocity dispersion and kinetic temperature) that we expect to vary consistently across trends in star formation.

Recent work on the Antennae (He et al. 2024) shows that  $\alpha_{\text{CO}}$  in this system has a negative correlation with their measurements of velocity dispersion. They make a similar argument that  $\alpha_{\text{CO}}$  may have a connection to the dynamics of the gas. He et al. (2024) find a strong, positive correlation between  $\alpha_{\text{CO}}$  and  $\tau_{\text{CO}}$ . We note that optical depth has a dependence on  $\sigma_v$  and gas surface density ( $\tau_{\text{CO}} \propto \sigma_v/\Sigma$ ). Thus, these results suggest some variations in the dynamics of the gas also impact CO optical depth, which is reflected in  $\alpha_{\text{CO}}$ . The importance of dynamics has also been discussed in earlier works by Solomon et al. (1987), and Solomon et al. (1997); Gao & Solomon (1999).

Work on the PHANGS galaxies at 150 pc scales shows there is a negative correlation between  $\alpha_{\text{CO}}$  and velocity dispersion which appears to have lower scatter ( $\sim 0.1$  dex) relative to previous prescriptions relying on gas or stellar surface density (Teng et al. 2024). They also argue that this correlation is tied to variations in emissivity of CO. We note that Teng et al. (2024) find a slightly steeper correlation than He et al. (2024) (slope  $-0.81$  vs.  $-0.46$ , respectively). When we fit this relationship in our models, we find a slope of  $\sim -0.5$ , more consistent with the Antennae relationship. When we estimate the scatter relative to our fit, we find  $\sim 0.16$  dex, similar that found by Teng et al. (2024),  $0.12$  dex. In summary, our models are able to reproduce the negative correlation between  $\alpha_{\text{CO}}$  and  $\sigma_v$  seen in high-resolution studies of PHANGS galaxies and the Antennae and can produce similar scatter. Furthermore, the physical origin of the variations in CO emissivity in the scatter of our models can be interpreted as

arising from variations in optical depth tied to the dynamics of the gas, analogous to what is observed across the Antennae and PHANGS galaxies (i.e. He et al. 2024; Teng et al. 2024).

Additionally, we find that uncertainties in CO emissivity can lead to different slopes in star formation scaling relations that can have significantly different implications. In Paper I, we find a discrepancy between the predictions of gravo-turbulent models of star formation and observations such that  $\epsilon_{\text{ff}}$  is predicted to increase with  $P_{\text{turb}}$  by these models, but observations instead show a decrease in  $\epsilon_{\text{ff}}$  with  $P_{\text{turb}}$ . We also show this in Fig. 10, where we plot the model-predicted  $\epsilon_{\text{ff}}$  as a function of  $P_{\text{turb}}$ , using the actual mean gas volume density to estimate  $t_{\text{ff}}$  and therefore  $\epsilon_{\text{ff}}$  (as well as  $P_{\text{turb}}$ ). In Paper I, we assume this discrepancy between our data and model predictions arises from uncertainties in mean volume density and our assumption that mean volume density scales with gas surface density (see Fig. 7 in Paper I). In Fig. 10, we show that all model estimates of  $t_{\text{dep}}$  as a function of the HCN/CO ratio have a negative trend, highlighting that this effect may be most important for observational relationships where subtle trends are expected. For example, the theoretical prediction for  $\epsilon_{\text{ff}}$  as a function of  $P_{\text{turb}}$  in our models has a slope of only  $\sim 0.05$ , and while our models (and data) show negative slopes around  $\sim -0.27$ . This comparison suggests that accurate pixel-by-pixel estimates of CO emissivity are required to derive much more accurate star formation scaling relations from observations. Such estimates can be derived via resolved studies of molecular line transitions with independent mass estimates, such as those derived from dust.

Finally, we plot  $t_{\text{dep,dense}}$  as a function of the HCN/CO ratio in Fig. 11 to consider how variations in HCN emissivity may impact observations of star formation relations. Interestingly, we do not see the same variation of the HCN emissivity in the scatter in  $t_{\text{dep,dense}}$  as a function of the HCN/CO ratio that we see in CO emissivity in Fig. 10. This is likely be-

cause variations in HCN emissivity are more strongly driven by HCN excitation, and only weakly driven by optical depth in our models. When we calculate the Spearman rank coefficient between  $\langle\alpha_{\text{HCN}}\rangle = 1/\langle\epsilon_{\text{HCN}}\rangle$  and the same parameters that we consider for CO, we find  $\alpha_{\text{HCN}}$  is strongly correlated ( $|r| \geq 0.95$ ) with  $\langle T_{\text{ex,HCN}}\rangle$ ,  $\sigma_v$ ,  $\Sigma$ ,  $n_0$ ,  $T_{\text{kin}}$ ,  $\langle I_{\text{HCN}}\rangle$  and only weakly correlated with  $\langle\tau_{\text{HCN}}\rangle$  ( $r = 0.21$ ). This further supports the idea that variations in HCN emissivity will not necessarily closely track variations in CO emissivity in observations.

Following our discussion in sections 3.2 (the HCN/CO ratio tracks the fraction of gas above  $n \gtrsim 10^{3.5} \text{ cm}^{-3}$ ) and 3.3 (application of a constant ratio in  $\alpha_{\text{HCN}}/\alpha_{\text{CO}}$  may still roughly yield  $f(n \gtrsim 10^{3.5} \text{ cm}^{-3})$ ), we consider how applying  $\langle\alpha_{\text{HCN}}\rangle = 3.2/\langle\epsilon_{\text{CO}}\rangle$  to  $I_{\text{HCN}}$  impacts the observed trend in  $t_{\text{dep,dense}}$  as a function of the HCN/CO ratio and how that compares to  $t_{\text{dep}}(n > 10^{3.5} \text{ cm}^{-3})$ . Assuming constant  $\alpha_{\text{HCN}}$ , the scatter in  $t_{\text{dep,dense}}$  as a function of the HCN/CO is  $\sim 0.21$  and becomes  $\sim 0.12$  when we apply  $\langle\alpha_{\text{HCN}}\rangle = 3.2/\langle\epsilon_{\text{CO}}\rangle$ . This scatter in the relationship between the predicted  $t_{\text{dep}}(n > 10^{3.5} \text{ cm}^{-3})$  and modelled HCN/CO ratio is  $\sim 0.18$ . When applying  $\langle\alpha_{\text{HCN}}\rangle = 3.2/\langle\epsilon_{\text{CO}}\rangle$ , the trend in  $t_{\text{dep,dense}}$  as a function of the HCN/CO agrees well with the predicted  $t_{\text{dep}}(n > 10^{3.5} \text{ cm}^{-3})$  and modelled HCN/CO ratio. To highlight this agreement, we also show a plot of  $t_{\text{dep,dense}}$  as a function of the HCN/CO ratio in Fig. 10 compared against depletion times of different fractions of gas, i.e.  $n > 10^{2.5}, 10^{3.5}, 10^{4.5}, 10^{5.5}, \text{ cm}^{-3}$ . Lower cuts in gas density produce shallow or negative relationships, while higher cuts produce steeper relationships. We also emphasize that the HCN/CO intensity ratio still appears to track a fairly constant fraction of gas, which in our models is at moderate gas densities ( $n > 10^{3.5} \text{ cm}^{-3}$ ). Thus, assuming a constant ratio in the conversion factors of HCN and CO, (e.g.  $\langle\alpha_{\text{HCN}}\rangle = 3.2/\langle\epsilon_{\text{CO}}\rangle$ ) may still be useful for determining the fraction of gas above this density.

We conclude that variations in HCN emissivity do not contribute significantly to the scatter of the considered star formation relationships. The scatter (in, e.g.  $\epsilon_{\text{ff}}$  and  $t_{\text{dep}}$  as a function of  $P_{\text{turb}}$  and  $t_{\text{dep,dense}}$  as a function of HCN/CO ratio) primarily originates from variations in gas velocity dispersion in our models, which has a stronger effect on CO emissivity relative to HCN emissivity. This does not exclude the possibility of variations in HCN emissivity occurring in the scatter of real observations. We do expect variations in HCN emissivity in the case where variations in the physical conditions of the gas (i.e. mean gas density and kinetic temperature) impact the excitation of HCN. Due to the strong dependence of HCN emissivity on excitation, it is necessary to perform multi-line studies of HCN to assess variations of this quantity. It still remains a challenge to determine a method for assessing the fraction of star-forming gas in molecular clouds in nearby galaxies, which may ultimately require highly resolved studies of star-forming gas clouds.

#### 4. Discussion & Conclusions

In this work we explore the properties of HCN and CO emission across a range of cloud models with realistic gas density distributions, and we combine the results of this analysis with the predictions of gravo-turbulent models of star formation. Our models use measurements of cloud properties based on observations of CO emission in nearby galaxies and incorporate a range of heating and cooling mechanisms to produce realistic gas temperatures (Sharda & Krumholz 2022). This prescription also includes the impact of radiation feedback from active star formation via the dust-gas energy exchange, which is important for star forming clouds (cf. Sharda & Krumholz 2022). Our models span

cloud properties found in Milky-Way type clouds (e.g. some of the PHANGS-type models of our study) through to more extreme cloud models, based on cloud properties measured in the Antennae and NGC3256. We also incorporate radiative transfer (RADEX, van der Tak et al. 2007) in order to calculate emissivities corresponding to these cloud models. This analysis allows us to constrain the impact of various physical properties (e.g. excitation, optical depth, mean density, velocity dispersion, temperature) on observed emission from CO and HCN across a broad range of galactic environments. Furthermore, we evaluate the sensitivity of the HCN-to-CO ratio to different gas densities, as well as to the fraction of gravitationally-bound, star-forming gas as predicted by analytic models of star formation (i.e. Burkhardt 2018; Burkhardt & Mocz 2019, which we use in this work, and also e.g. Krumholz & McKee 2005; Federrath & Klessen 2012; Hennebelle & Chabrier 2011; Burkhardt 2018, for which the results are still broadly applicable). Below we provide an itemized summary as well as a brief discussion of the primary scientific results from this work.

1. Simple models of clouds that combine realistic gas volume density distributions with radiative transfer are successful at reproducing observed  $I_{\text{HCN}}/I_{\text{CO}}$  ratios (cf. Section 2 and Figs. 1 and 3; see also Leroy et al. 2017b; Shirley 2015). Furthermore, they are successful at reproducing CO and HCN emissivities, optical depths, and trends in excitation that have been constrained from numerical work (cf. Section 3.1 and Figs. 4 and 5; Narayanan et al. 2012; Narayanan & Krumholz 2014; Gong et al. 2020; Hu et al. 2022a). Additionally, we find agreement between the trends in our model CO and HCN emissivities as a function of CO and HCN intensity and observationally-derived values of the CO and HCN conversion factors in nearby galaxies and Milky Way clouds (cf. Section 3.3 and Fig 7; Teng et al. 2024; He et al. 2024; Dame & Lada 2023; Shimajiri et al. 2017; Tafalla et al. 2023).
2.  $I_{\text{HCN}}/I_{\text{CO}}$  is linearly correlated with the fraction of gas above moderate gas densities, e.g.  $n \sim 10^{3.5} \text{ cm}^{-3}$ , and the relationship between  $I_{\text{HCN}}/I_{\text{CO}}$  and the fraction of *dense* gas above  $n \sim 10^{4.5} \text{ cm}^{-3}$  is sublinear in our models (cf. Section 3.2 and Fig. 6). Thus, our models predict that  $I_{\text{HCN}}/I_{\text{CO}}$  is tracing the fraction of gas above a roughly constant, moderate gas density, in agreement with the results of previous studies (e.g. Kauffmann et al. 2017; Pety et al. 2017), and this ratio is still useful in the determination of the fraction of gas above moderate densities (cf. Fig. 11). One can still apply a roughly constant ratio in the HCN and CO conversion factors to  $I_{\text{HCN}}/I_{\text{CO}}$  to estimate, e.g.  $f(n \sim 10^{3.5} \text{ cm}^{-3})$ . This is roughly  $\alpha_{\text{HCN}}/\alpha_{\text{CO}} \approx 5$  in our models.
3. The modelled  $I_{\text{HCN}}/I_{\text{CO}}$  and HCN/CO emissivity ratios are negatively correlated with  $f_{\text{grav}}$ , as predicted by gravo-turbulent models of star formation with varying star formation thresholds (cf. Section 3.4 and Fig. 9). Thus, models with the lowest estimates of  $f_{\text{grav}}$  appear to have the highest dense gas fractions, i.e.  $f(n > 10^{4.5} \text{ cm}^{-3})$  and highest  $I_{\text{HCN}}/I_{\text{CO}}$ . We find that  $f_{\text{grav}}$  is predicted to decrease from 1.7% in the PHANGS-type models to 0.8% and 0.6% in the NGC4038/9- and NGC3256-type models, respectively. In contrast to this, the fraction of *dense* gas above  $n = 10^{4.5} \text{ cm}^{-3}$  increases from 1.9% in the PHANGS-type models to 22% and 30% in the NGC4038/9- and NGC3256-type models, respectively. The transition density (the density at which gas becomes self-gravitating in our models) increases across our model parameter space from  $n = 10^{4.5} \text{ cm}^{-3}$  in the

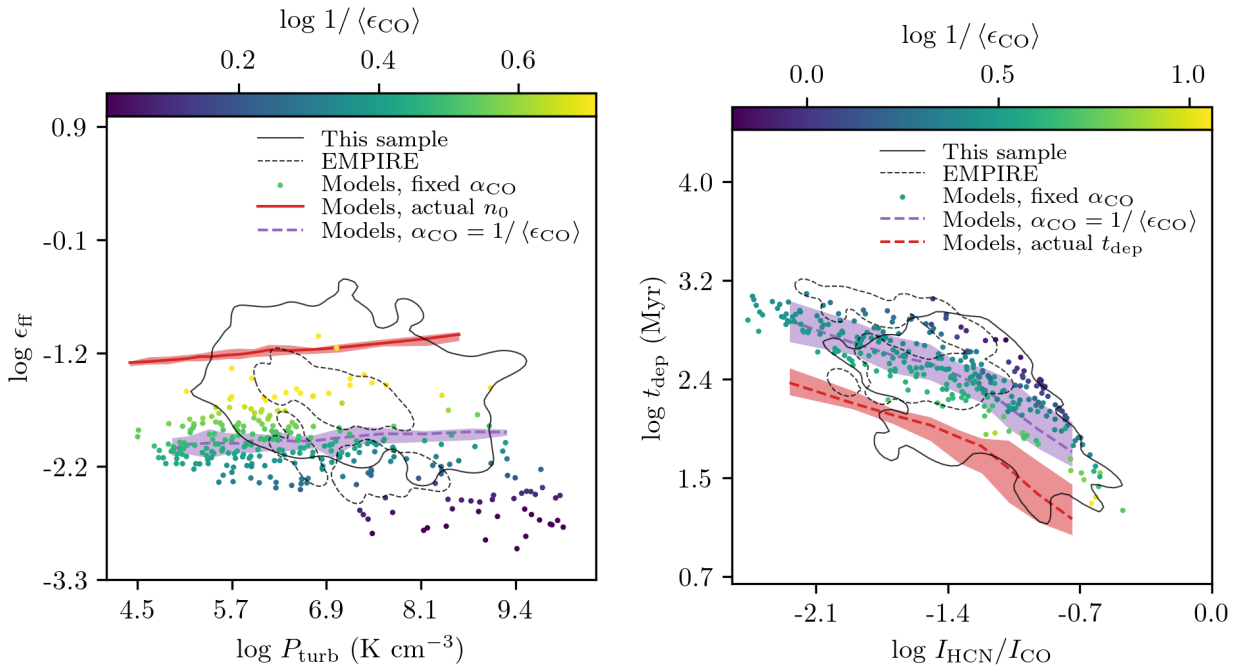


**Fig. 10.** *Left:* Model efficiency per free-fall time as a function of turbulent pressure shown three ways: (1) using modelled  $I_{\text{CO}}$  and a fixed CO conversion factor for gas surface density estimates (color points), (2) using the actual theoretical  $\epsilon_{\text{ff}}$  and  $P_{\text{turb}}$  values (red line), and (3) using modelled  $I_{\text{CO}}$  with  $\langle\alpha_{\text{CO}}\rangle = 1/\langle\epsilon_{\text{CO}}\rangle$  (purple trend line). Shaded regions represent the full range of model scatter. Estimates of these quantities from our sample of galaxies and the EMPIRE sample are shown as the solid black and dashed black contours, respectively. *Right:* Model depletion time as a function of HCN/CO ratio shown three ways, using the same approach. We find that the scatter produced by variations in CO emissivity can account for a significant portion of the scatter seen in observations. Additionally, the trend in  $\epsilon_{\text{ff}}$  with  $P_{\text{turb}}$  is dependent on the assumed CO conversion factor. Pixel-by-pixel estimates of  $\alpha_{\text{CO}}$  may be necessary for accurate studies of star formation trends. We note that the offset in  $\epsilon_{\text{ff}}$  and  $t_{\text{dep}}$  between methods (2) and (3) is a result of modelled CO emission missing a fraction of the lower surface density gas in our models, to “CO-dark” gas.

PHANGS-type models to  $n = 10^{5.9} \text{ cm}^{-3}$  and  $n = 10^{6.6} \text{ cm}^{-3}$  in the NGC4038/9- and NGC3256-type models, respectively. Thus, in the PHANGS-type models  $f_{\text{grav}}$  is well-matched to  $f_{\text{dense}}$ , and the transition density for the PHANGS-type models agrees well with the estimation for the threshold density for star formation in the Milky Way (e.g.  $n \gtrsim 10^4 \text{ cm}^{-3}$ , cf. Section 3.4, Lada et al. 2010, 2012).

4. Models with the lowest estimates of  $f_{\text{grav}}$  (highest  $f(n > 10^{4.5} \text{ cm}^{-3})$ ) and highest  $I_{\text{HCN}}/I_{\text{CO}}$  appear to have the *shortest* gas depletion times (i.e. the NGC4038/9- and NGC3256-type models). Thus, smaller  $f_{\text{grav}}$  does not necessarily mean longer depletion times in the case where sufficient mass is available to star formation. We find the trend in the modelled gas depletion times and  $I_{\text{HCN}}/I_{\text{CO}}$  are consistent with the trend observed in our data (cf. Section 3.4 and Fig. 9).
5. The scatter observed in star formation trends, such as  $\epsilon_{\text{ff}}$  and  $t_{\text{dep}}$  as a function of  $P_{\text{turb}}$  and HCN/CO ratio, can largely be attributed to variations in CO emissivity. We find the scatter in these relationships are reduced by a factor of  $\sim 2 - 3$  when we apply modelled CO emissivity to  $I_{\text{CO}}$  to estimate gas surface density (relative to the assumption of a fixed CO conversion factor). We find variations in CO emissivity are primarily driven by variations in the optical depth of CO due to the dynamics of the gas (cf. Section 3.5 and Fig. 10). We do not see the same variations in HCN emissivity in the scatter of  $t_{\text{dep,dense}}$  as a function of HCN/CO ratio, and find that HCN emissivity is more strongly correlated with excitation. Thus, variations in HCN and CO emissivity have different physical origins according to our models (cf. Figs. 9 and 11).

6. The assumption of constant conversion factors can alter the slope of star formation trends, which is most important for trends with subtle slopes. For example, we find the assumption of a constant CO conversion factor can produce a negative trend in  $\epsilon_{\text{ff}}$  with turbulent pressure (slope  $\sim -0.27$ ) in our models that also agrees with the negative trend we find in our sample in Paper I. Our models predict the actual trend in  $\epsilon_{\text{ff}}$  with turbulent pressure is marginally positive, ( $\sim 0.05$ , cf. Fig. 10).

A key prediction of our models is that, on average,  $I_{\text{HCN}}/I_{\text{CO}}$  does appear to track gas above a relatively fixed density. However, this fraction includes more moderately dense gas (i.e.  $n > 10^{3.5} \text{ cm}^{-3}$ ) as opposed to strictly dense gas above  $n > 10^{4.5} \text{ cm}^{-3}$ . This conclusion generally agrees with more recent studies of HCN emission in Milky Way clouds that find HCN emission includes more moderate gas densities (e.g. Kauffmann et al. 2017; Pety et al. 2017). We find evidence that  $I_{\text{HCN}}/I_{\text{CO}}$  tracks a gas fraction including more moderate gas densities even in the more extreme environments. This analysis implies that previous estimates of dense gas fractions likely overestimate the true fraction of gas above  $n > 10^{4.5}$ .

Furthermore, we show that the fraction of gravitationally-bound gas, as predicted by turbulent models of star formation (i.e. Burkhardt 2018; Burkhardt & Mocz 2019, which we use in this work, and also e.g. Krumholz & McKee 2005; Federrath & Klessen 2012; Hennebelle & Chabrier 2011; Burkhardt 2018), decreases with  $I_{\text{HCN}}/I_{\text{CO}}$ . This result agrees with Paper I, and combined with the subthermal excitation of HCN, suggests that it may not be appropriate to interpret  $I_{\text{HCN}}/I_{\text{CO}}$  as a straight-



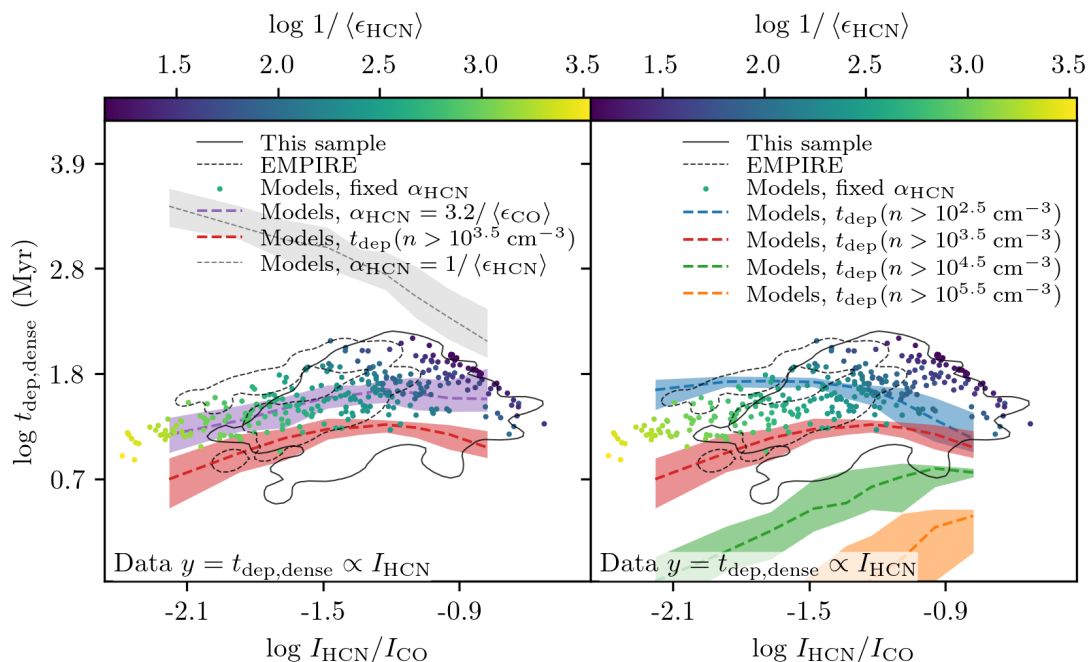


**Fig. 11.** *Left:* Model dense gas depletion time as a function of HCN/CO ratio shown three ways: (1) using modelled  $I_{\text{HCN}}$  and a fixed HCN conversion factor for gas surface density estimates (color points), (2) using the theoretical depletion time of the fraction of gas above  $n > 10^{3.5} \text{ cm}^{-3}$  (red line), and (3) using modelled  $I_{\text{HCN}}$  with  $\langle\alpha_{\text{HCN}}\rangle = 3.2\langle\alpha_{\text{CO}}\rangle$  applied to estimate dense gas surface density (purple line). We also show the resulting trend using modelled  $I_{\text{HCN}}$  with  $\langle\alpha_{\text{HCN}}\rangle = 1/\langle\epsilon_{\text{HCN}}\rangle$  (gray dashed line) for comparison. *Right:* We plot the model dense gas depletion time as a function of HCN/CO ratio shown three ways, this time overlaying depletion times of several fractions of gas: i.e. that above  $n > 10^{2.5}, 10^{3.5}, 10^{4.5}, 10^{5.5}, \text{ cm}^{-3}$  (blue, red, green, and orange lines, respectively) as a function of HCN/CO ratio. Shaded regions represent the full range of model scatter. We find that the HCN emissivity does not appear to contribute to the scatter of these relationships in the way that CO contributes to those in Fig. 10, which is likely due to the stronger dependence of HCN emissivity on excitation relative to optical depth. Additionally, the trend in dense gas depletion time with the HCN/CO ratio depends critically on the assumed HCN conversion factor. This figure also demonstrates that the HCN emissivity does not necessarily track the mass of star-forming gas (gray trend in the left panel), but that applying  $\langle\alpha_{\text{HCN}}\rangle = 3.2\langle\alpha_{\text{CO}}\rangle$  to  $I_{\text{HCN}}$  when estimating “ $t_{\text{dep,dense}}$ ” does a reasonable job at reproducing the depletion time of gas above moderate gas densities (red lines, both panels; see also Figs. 6 and 7 and Section 3.4).

forward tracer of the dense gas associated with ongoing star formation in galaxies. While  $I_{\text{HCN}}/I_{\text{CO}}$  does scale with the fraction of moderate to high density gas, this is not necessarily equivalent to the fraction of gas contributing to star formation, especially in more extreme environments.

A critical observational uncertainty in the study of gas traced by HCN in extragalactic systems is the lack of observational constraints on the HCN conversion factor. Most observational prescriptions assume that HCN is optically thick, but as we show with our modelling, HCN appears only moderately thick, and these findings are consistent with the study of HCN and  $\text{H}^{13}\text{CN}$  in the centers of nearby galaxies (Jiménez-Donaire et al. 2017). Additionally, we also show that HCN is primarily subthermally excited, which also agrees with the recent findings of HCN emission in Perseus by Dame & Lada (2023). Despite these complications, it may still be possible to use HCN as a tracer of dense gas. Recent work shows that on galactic scales, the ratio between HCN and  $\text{N}_2\text{H}^+$  is nearly constant (Jiménez-Donaire et al. 2023). Since  $\text{N}_2\text{H}^+$  has been shown to be a tracer of even denser gas than that traced by HCN (Kauffmann et al. 2017; Pety et al. 2017; Priestley et al. 2023), it may indicate that it is still possible to calibrate a conversion between HCN luminosity and total dense gas mass in molecular clouds.

One potential limitation of the use of an HCN conversion factor is if the fraction of dense gas mass does not increase linearly with the total mass of molecular clouds. Our models show that the ratio between the CO and HCN conversion fac-

tors,  $\alpha_{\text{HCN}}/\alpha_{\text{CO}}$ , would need to increase with  $I_{\text{HCN}}/I_{\text{CO}}$  for  $I_{\text{HCN}}$  to accurately trace the fraction of gas  $n > 10^{4.5} \text{ cm}^{-3}$  predicted by an  $n$  – PDF with both a lognormal and powerlaw component. This result needs to be confirmed through more resolved studies of molecular clouds, particularly in the Milky Way. It is crucial to map the density structure down to small scales in clouds and directly compare this with mappings of multiple molecular line transitions over a range of cloud types (e.g. Dame & Lada 2023; Tafalla et al. 2023; Shimajiri et al. 2017). Including an analysis of the distribution of gas densities can also shed light on the physics of molecular clouds, and how much dense star-forming gas there is in relation to various molecular line emissivities. Additionally, multi-line studies targeting higher-J transitions are necessary to constrain the mean volume density and gas temperature traced by a particular molecular species, which are also important for determining total gas masses.

*Acknowledgements.* Part of this work was supported by an Ontario Trillium Scholarship (2015-2019). The research of CDW is supported by grants from the Natural Sciences and Engineering Research Council of Canada and the Canada Research Chairs program. PS is supported by the Leiden University Oort Fellowship and the International Astronomical Union – Gruber Foundation Fellowship. IDR is supported by the Banting Fellowship program. This paper makes use of the following ALMA data: ADS/JAO.ALMA#2011.0.00467.S, ADS/JAO.ALMA#2011.0.00525.S, ADS/JAO.ALMA#2011.0.00772.S, ADS/JAO.ALMA#2012.1.00165.S, ADS/JAO.ALMA#2012.1.01004.S, ADS/JAO.ALMA#2012.1.00185.S, ADS/JAO.ALMA#2013.1.00247.S, ADS/JAO.ALMA#2013.1.00634.S, ADS/JAO.ALMA#2013.1.00885.S, ADS/JAO.ALMA#2013.1.00911.S, ADS/JAO.ALMA#2013.1.01057.S, ADS/JAO.ALMA#2015.1.00993.S.

- ADS/JAO.ALMA#2015.1.01177.S, ADS/JAO.ALMA#2015.1.01286.S, ADS/JAO.ALMA#2015.1.01538.S. ALMA is a partnership of ESO (representing its member states), NSF (USA) and NINS (Japan), together with NRC (Canada), MOST and ASIAA (Taiwan), and KASI (Republic of Korea), in cooperation with the Republic of Chile. The Joint ALMA Observatory is operated by ESO, AUI/NRAO and NAOJ. *Software*: This work made use of the following software: RADEX (van der Tak et al. 2007), ASTROPY (Astropy Collaboration et al. 2013, 2018, 2022), PANDAS (Wes McKinney 2010; pandas development team 2020), MATPLOTLIB (Hunter 2007), NUMPY (Harris et al. 2020), and SCIPY (Virtanen et al. 2020).
- ## References
- Aladro, R., Martín, S., Riquelme, D., et al. 2015, *A&A*, 579, A101  
 Ao, Y., Henkel, C., Menten, K. M., et al. 2013, *A&A*, 550, A135  
 Astropy Collaboration, Price-Whelan, A. M., Lim, P. L., et al. 2022, *ApJ*, 935, 167  
 Astropy Collaboration, Price-Whelan, A. M., Sipőcz, B. M., et al. 2018, *AJ*, 156, 123  
 Astropy Collaboration, Robitaille, T. P., Tollerud, E. J., et al. 2013, *A&A*, 558, A33  
 Bacchini, C., Fraternali, F., Iorio, G., & Pezzulli, G. 2019, *A&A*, 622, A64  
 Ballesteros-Paredes, J., Vázquez-Semadeni, E., Gazol, A., et al. 2011, *MNRAS*, 416, 1436  
 Barnes, A. T., Kauffmann, J., Bigiel, F., et al. 2020, *MNRAS*, 497, 1972  
 Barnes, J. E. & Hernquist, L. 1996, *ApJ*, 471, 115  
 Beattie, J. R., Mocz, P., Federrath, C., & Klessen, R. S. 2021, *MNRAS*, 504, 4354  
 Beetz, C., Schwarz, C., Dreher, J., & Grauer, R. 2008, *Physics Letters A*, 372, 3037  
 Bemis, A. & Wilson, C. D. 2019, *AJ*, 157, 131  
 Bemis, A. R. & Wilson, C. D. 2023, *ApJ*, 945, 42  
 Bešlić, I., Barnes, A. T., Bigiel, F., et al. 2021, *MNRAS*, 506, 963  
 Bigiel, F., Leroy, A., Walter, F., et al. 2008, *AJ*, 136, 2846  
 Bigiel, F., Leroy, A. K., Blitz, L., et al. 2015, *ApJ*, 815, 103  
 Bolatto, A. D., Wolfire, M., & Leroy, A. K. 2013, *ARAA*, 51, 207  
 Bournaud, F., Duc, P. A., & Emsellem, E. 2008, *MNRAS*, 389, L8  
 Brunetti, N. & Wilson, C. D. 2022, *MNRAS*, 515, 2928  
 Brunetti, N., Wilson, C. D., He, H., et al. 2024, *MNRAS*, 530, 597  
 Brunetti, N., Wilson, C. D., Sliwa, K., et al. 2021, *MNRAS*, 500, 4730  
 Brunt, C. M. 2010, *A&A*, 513, A67  
 Brunt, C. M., Federrath, C., & Price, D. J. 2010a, *MNRAS*, 405, L56  
 Brunt, C. M., Federrath, C., & Price, D. J. 2010b, *MNRAS*, 403, 1507  
 Burkhardt, B. 2018, *ApJ*, 863, 118  
 Burkhardt, B. & Lazarian, A. 2012, *ApJ*, 755, L19  
 Burkhardt, B. & Mocz, P. 2019, *ApJ*, 879, 129  
 Burkhardt, B., Ossenkopf, V., Lazarian, A., & Stutzki, J. 2013, *ApJ*, 771, 122  
 Burkhardt, B., Stalpes, K., & Collins, D. C. 2017, *ApJ*, 834, L1  
 Burkhardt, B., Stanimirović, S., Lazarian, A., & Kowal, G. 2010, *ApJ*, 708, 1204  
 Caselli, P. & Ceccarelli, C. 2012, *A&A Rev.*, 20, 56  
 Chakrabarti, S. & McKee, C. F. 2005, *ApJ*, 631, 792  
 Chen, H., Gao, Y., Braine, J., & Gu, Q. 2015, *ApJ*, 810, 140  
 Chen, H. H.-H., Pineda, J. E., Offner, S. S. R., et al. 2019, *ApJ*, 886, 119  
 Choudhury, S., Pineda, J. E., Caselli, P., et al. 2021, *A&A*, 648, A114  
 Crocker, R. M., Krumholz, M. R., & Thompson, T. A. 2021, *MNRAS*, 503, 2651  
 Dame, T. M. & Lada, C. J. 2023, *ApJ*, 944, 197  
 Dib, S., Brandenburg, A., Kim, J., Gopinathan, M., & André, P. 2008, *ApJ*, 678, L105  
 Downes, D., Solomon, P. M., & Radford, S. J. E. 1993, *ApJ*, 414, L13  
 Draine, B. T. 2011, *Physics of the Interstellar and Intergalactic Medium*  
 Eibensteiner, C., Barnes, A. T., Bigiel, F., et al. 2022, *A&A*, 659, A173  
 Elmegreen, B. G. 2011, *ApJ*, 731, 61  
 Elmegreen, B. G. & Falgarone, E. 1996, *ApJ*, 471, 816  
 Elmegreen, B. G. & Scalo, J. 2004, *ARA&A*, 42, 211  
 Federrath, C. & Banerjee, S. 2015, *MNRAS*, 448, 3297  
 Federrath, C. & Klessen, R. S. 2012, *ApJ*, 761, 156  
 Federrath, C. & Klessen, R. S. 2013, *ApJ*, 763, 51  
 Federrath, C., Klessen, R. S., & Schmidt, W. 2008, *ApJ*, 688, L79  
 Federrath, C., Rathborne, J. M., Longmore, S. N., et al. 2016a, *ApJ*, 832, 143  
 Federrath, C., Rathborne, J. M., Longmore, S. N., et al. 2016b, *ApJ*, 832, 143  
 Federrath, C., Roman-Duval, J., Klessen, R. S., Schmidt, W., & Mac Low, M. M. 2010, *A&A*, 512, A81  
 Field, G. B., Blackman, E. G., & Keto, E. R. 2011, *MNRAS*, 416, 710  
 Fleck, R. C., J. & Clark, F. O. 1981, *ApJ*, 245, 898  
 Forbrich, J., Lada, C. J., Pety, J., & Petitpas, G. 2023, *arXiv e-prints*, arXiv:2308.12906  
 Foster, J. B., Rosolowsky, E. W., Kauffmann, J., et al. 2009, *ApJ*, 696, 298  
 Friesen, R. K. & Jarvis, E. 2024, *ApJ*, 969, 70  
 Friesen, R. K., Pineda, J. E., co-PIs, et al. 2017, *ApJ*, 843, 63  
 Gallagher, M. J., Leroy, A. K., Bigiel, F., et al. 2018a, *ApJ*, 868, L38  
 Gallagher, M. J., Leroy, A. K., Bigiel, F., et al. 2018b, *ApJ*, 858, 90  
 Gao, Y. & Solomon, P. M. 1999, *ApJ*, 512, L99  
 Gao, Y. & Solomon, P. M. 2004a, *ApJS*, 152, 63  
 Gao, Y. & Solomon, P. M. 2004b, *ApJ*, 606, 271  
 García-Burillo, S., Usero, A., Alonso-Herrero, A., et al. 2012, *A&A*, 539, A8  
 García-Rodríguez, A., Usero, A., Leroy, A. K., et al. 2023, *A&A*, 672, A96  
 Gerrard, I. A., Federrath, C., Pingel, N. M., et al. 2023, *MNRAS*, 526, 982  
 Gerrard, I. A., Noon, K. A., Federrath, C., et al. 2024, *MNRAS*, 530, 4317  
 Ginsburg, A., Federrath, C., & Darling, J. 2013, *ApJ*, 779, 50  
 Ginsburg, A., Henkel, C., Ao, Y., et al. 2016, *A&A*, 586, A50  
 Glover, S. C. O. & Mac Low, M.-M. 2007a, *ApJS*, 169, 239  
 Glover, S. C. O. & Mac Low, M.-M. 2007b, *ApJ*, 659, 1317  
 Gong, M., Ostriker, E. C., Kim, C.-G., & Kim, J.-G. 2020, *ApJ*, 903, 142  
 Goodman, A. A., Benson, P. J., Fuller, G. A., & Myers, P. C. 1993, *ApJ*, 406, 528  
 Graciá-Carpio, J., Garcá-Burillo, S., Planesas, P., Fuente, A., & Usero, A. 2008, *A&A*, 479, 703  
 Harris, C. R., Millman, K. J., van der Walt, S. J., et al. 2020, *Nature*, 585, 357  
 He, H., Wilson, C., Sun, J., Teng, Y.-H., & Rosolowsky, E. 2024, *arXiv e-prints*, arXiv:2401.16476  
 Hennebelle, P. & Chabrier, G. 2011, *ApJ*, 743, L29  
 Henshaw, J. D., Longmore, S. N., Kruijssen, J. M. D., et al. 2016, *MNRAS*, 457, 2675  
 Heyer, M. & Dame, T. M. 2015, *ARAA*, 53, 583  
 Heyer, M., Krawczyk, C., Duval, J., & Jackson, J. M. 2009, *ApJ*, 699, 1092  
 Ho, P. T. P. & Townes, C. H. 1983, *ARA&A*, 21, 239  
 Hopkins, P. F. 2013, *MNRAS*, 430, 1653  
 Hu, C.-Y., Schrubba, A., Sternberg, A., & van Dishoeck, E. F. 2022a, *ApJ*, 931, 28  
 Hu, Z., Krumholz, M. R., Pokhrel, R., & Gutermuth, R. A. 2022b, *MNRAS*, 511, 1431  
 Hunter, J. D. 2007, *Computing in Science & Engineering*, 9, 90  
 Jiménez-Donaire, M. J., Bigiel, F., Leroy, A. K., et al. 2017, *MNRAS*, 466, 49  
 Jiménez-Donaire, M. J., Bigiel, F., Leroy, A. K., et al. 2019, *ApJ*, 880, 127  
 Jiménez-Donaire, M. J., Usero, A., Bešlić, I., et al. 2023, *A&A*, 676, L11  
 Jones, P. A., Burton, M. G., Cunningham, M. R., et al. 2012, *MNRAS*, 419, 2961  
 Kainulainen, J., Beuther, H., Henning, T., & Plume, R. 2009, *A&A*, 508, L35  
 Kainulainen, J. & Federrath, C. 2017, *A&A*, 608, L3  
 Kainulainen, J., Federrath, C., & Henning, T. 2014, *Science*, 344, 183  
 Kainulainen, J. & Tan, J. C. 2013, *A&A*, 549, A53  
 Kauffmann, J., Bertoldi, F., Bourke, T. L., Evans, N. J., I., & Lee, C. W. 2008, *A&A*, 487, 993  
 Kauffmann, J., Goldsmith, P. F., Melnick, G., et al. 2017, *A&A*, 605, L5  
 Khullar, S., Krumholz, M. R., Federrath, C., & Cunningham, A. J. 2019, *MNRAS*, 488, 1407  
 Kim, T., Gadotti, D. A., Querejeta, M., et al. 2024, *arXiv e-prints*, arXiv:2405.00107  
 Konstantin, L., Girichidis, P., Federrath, C., & Klessen, R. S. 2012, *ApJ*, 761, 149  
 Kruijssen, J. M. D., Longmore, S. N., Elmegreen, B. G., et al. 2014, *MNRAS*, 440, 3370  
 Krumholz, M. R. 2011, *ApJ*, 743, 110  
 Krumholz, M. R., Crocker, R. M., & Offner, S. S. R. 2023, *MNRAS*, 520, 5126  
 Krumholz, M. R. & McKee, C. F. 2005, *ApJ*, 630, 250  
 Lada, C. J., Forbrich, J., Lombardi, M., & Alves, J. F. 2012, *ApJ*, 745, 190  
 Lada, C. J., Lombardi, M., & Alves, J. F. 2010, *ApJ*, 724, 687  
 Lang, P., Meidt, S. E., Rosolowsky, E., et al. 2020, *ApJ*, 897, 122  
 Larson, R. B. 1981, *MNRAS*, 194, 809  
 Leroy, A. K., Schinnerer, E., Hughes, A., et al. 2017a, *ApJ*, 846, 71  
 Leroy, A. K., Usero, A., Schrubba, A., et al. 2017b, *ApJ*, 835, 217  
 Longmore, S. N., Bally, J., Testi, L., et al. 2013, *MNRAS*, 429, 987  
 Marchal, A. & Miville-Deschênes, M.-A. 2021, *ApJ*, 908, 186  
 Mauersberger, R. & Henkel, C. 1991, *A&A*, 245, 457  
 Meier, D. S. & Turner, J. L. 2005, *ApJ*, 618, 259  
 Menon, S. H., Federrath, C., Klaassen, P., Kuiper, R., & Reiter, M. 2021, *MNRAS*, 500, 1721  
 Mills, E. A. C. 2017, *arXiv e-prints*, arXiv:1705.05332  
 Miville-Deschênes, M.-A., Murray, N., & Lee, E. J. 2017, *ApJ*, 834, 57  
 Molina, F. Z., Glover, S. C. O., Federrath, C., & Klessen, R. S. 2012, *MNRAS*, 423, 2680  
 Myers, P. C., Ladd, E. F., & Fuller, G. A. 1991, *ApJ*, 372, L95  
 Narayanan, D. & Krumholz, M. R. 2014, *MNRAS*, 442, 1411  
 Narayanan, D., Krumholz, M. R., Ostriker, E. C., & Hernquist, L. 2012, *MNRAS*, 421, 3127  
 Neumann, L., Gallagher, M. J., Bigiel, F., et al. 2023, *MNRAS*, 521, 3348  
 Nguyen, Q. R., Jackson, J. M., Henkel, C., Truong, B., & Mauersberger, R. 1992, *ApJ*, 399, 521  
 Nishimura, Y., Shimonishi, T., Watanabe, Y., et al. 2016, *ApJ*, 818, 161

- Nolan, C. A., Federrath, C., & Sutherland, R. S. 2015, MNRAS, 451, 1380
- Onus, A., Krumholz, M. R., & Federrath, C. 2018, MNRAS, 479, 1702
- Padoan, P., Jones, B. J. T., & Nordlund, Å. P. 1997, ApJ, 474, 730
- Padoan, P. & Nordlund, Å. 2011, ApJ, 730, 40
- Pan, L. & Padoan, P. 2009, ApJ, 692, 594
- Pan, L., Padoan, P., Haugbølle, T., & Nordlund, Å. 2016, ApJ, 825, 30
- pandas development team, T. 2020, pandas-dev/pandas: Pandas
- Parmentier, G. 2014, Astronomische Nachrichten, 335, 543
- Parmentier, G. 2019, ApJ, 887, 179
- Passot, T. & Vázquez-Semadeni, E. 1998, Phys. Rev. E, 58, 4501
- Pety, J., Guzmán, V. V., Orkisz, J. H., et al. 2017, A&A, 599, A98
- Pineda, J. E., Goodman, A. A., Arce, H. G., et al. 2010, ApJ, 712, L116
- Price, D. J., Federrath, C., & Brunt, C. M. 2011, ApJ, 727, L21
- Priestley, F. D., Clark, P. C., Glover, S. C. O., et al. 2023, MNRAS, 524, 5971
- Querejeta, M., Schinnerer, E., Schruha, A., et al. 2019, A&A, 625, A19
- Rathborne, J. M., Longmore, S. N., Jackson, J. M., et al. 2014, ApJ, 795, L25
- Renaud, F., Bournaud, F., Kraljic, K., & Duc, P.-A. 2014, MNRAS, 442, L33
- Rosolowsky, E., Hughes, A., Leroy, A. K., et al. 2021, MNRAS, 502, 1218
- Rosolowsky, E. & Leroy, A. 2006, PASP, 118, 590
- Sakamoto, K., Aalto, S., Evans, A. S., Wiedner, M. C., & Wilner, D. J. 2010, ApJ, 725, L228
- Salim, D. M., Federrath, C., & Kewley, L. J. 2015, ApJ, 806, L36
- Sandstrom, K. M., Leroy, A. K., Walter, F., et al. 2013, ApJ, 777, 5
- Santa-Maria, M. G., Goicoechea, J. R., Pety, J., et al. 2023, A&A, 679, A4
- Schinnerer, E. & Leroy, A. K. 2024, ARA&A, 62, 369
- Schneider, N., Bontemps, S., Simon, R., et al. 2011, A&A, 529, A1
- Schneider, N., Ossenkopf-Okada, V., Clarke, S., et al. 2022, A&A, 666, A165
- Schruha, A., Leroy, A. K., Walter, F., et al. 2012, AJ, 143, 138
- Sharda, P., Federrath, C., da Cunha, E., Swinbank, A. M., & Dye, S. 2018, MNRAS, 477, 4380
- Sharda, P. & Krumholz, M. R. 2022, MNRAS, 509, 1959
- Shima, K., Tasker, E. J., & Habe, A. 2017, MNRAS, 467, 512
- Shimajiri, Y., André, P., Braine, J., et al. 2017, A&A, 604, A74
- Shirley, Y. L. 2015, PASP, 127, 299
- Shu, F. H. 1977, ApJ, 214, 488
- Sliwa, K., Wilson, C. D., Matsushita, S., et al. 2017, ApJ, 840, 8
- Sokolov, V., Wang, K., Pineda, J. E., et al. 2019, ApJ, 872, 30
- Solomon, P. M., Downes, D., Radford, S. J. E., & Barrett, J. W. 1997, ApJ, 478, 144
- Solomon, P. M., Rivolo, A. R., Barrett, J., & Yahil, A. 1987, ApJ, 319, 730
- Squire, J. & Hopkins, P. F. 2017, MNRAS, 471, 3753
- Sun, J., Leroy, A. K., Ostriker, E. C., et al. 2020, ApJ, 892, 148
- Sun, J., Leroy, A. K., Schruha, A., et al. 2018, ApJ, 860, 172
- Szűcs, L., Glover, S. C. O., & Klessen, R. S. 2016, MNRAS, 460, 82
- Tafalla, M., Usero, A., & Hacar, A. 2021, A&A, 646, A97
- Tafalla, M., Usero, A., & Hacar, A. 2023, A&A, 679, A112
- Takano, S., Nakajima, T., & Kohno, K. 2019, PASJ, 71, S20
- Tan, J. C., Krumholz, M. R., & McKee, C. F. 2006, ApJ, 641, L121
- Teng, Y.-H., Chiang, I.-D., Sandstrom, K. M., et al. 2024, ApJ, 961, 42
- Usero, A., Leroy, A. K., Walter, F., et al. 2015, AJ, 150, 115
- Utomo, D., Blitz, L., Davis, T., et al. 2015, ApJ, 803, 16
- Utomo, D., Sun, J., Leroy, A. K., et al. 2018, ApJ, 861, L18
- van der Tak, F. F. S., Black, J. H., Schöier, F. L., Jansen, D. J., & van Dishoeck, E. F. 2007, A&A, 468, 627
- Virtanen, P., Gommers, R., Oliphant, T. E., et al. 2020, Nature Methods, 17, 261
- Viti, S. 2017, A&A, 607, A118
- Walker, D. L., Longmore, S. N., Zhang, Q., et al. 2018, MNRAS, 474, 2373
- Watanabe, Y., Sakai, N., Sorai, K., & Yamamoto, S. 2014, ApJ, 788, 4
- Wes McKinney. 2010, in Proceedings of the 9th Python in Science Conference, ed. Stéfan van der Walt & Jarrod Millman, 56 – 61
- Wilson, C. D., Bemis, A., Ledger, B., & Klimi, O. 2023, MNRAS, 521, 717
- Wilson, C. D., Elmegreen, B. G., Bemis, A., & Brunetti, N. 2019, ApJ, 882, 5
- Wolfire, M. G., Hollenbach, D., & McKee, C. F. 2010, ApJ, 716, 1191
- Yue, N.-N., Li, D., Zhang, Q.-Z., et al. 2021, Research in Astronomy and Astrophysics, 21, 024
- Yun, H.-S., Lee, J.-E., Choi, Y., et al. 2021, ApJS, 256, 16



## Appendix A: Molecular Line Velocity Dispersion as a Measure of Mach Number

In this section we discuss how velocity dispersion from measured line emission may be connected to mach number in gas clouds, as this is an assumption of our models.

### Appendix A.1: Observational Evidence for the $\sigma_{n/n_0}^2$ - $\mathcal{M}$ Relation

Comparisons between independent measurements of  $\sigma_{n/n_0}^2$  and  $\mathcal{M}$  in resolved studies of clouds provide crucial tests to these theories. Studies focusing on clouds in the Solar neighborhood only find weak observational evidence of a scaling between the 2D gas density variance and velocity dispersion derived from molecular transitions (e.g. [Kainulainen et al. 2009](#); [Kainulainen & Tan 2013](#)), which may in part be due the uncertainty in confounding factors, such as  $b$  (i.e. [Kainulainen & Federrath 2017](#)). Alternatively, this may be due to lack of dynamic range in  $\mathcal{M}$  in Solar neighborhood clouds; a stronger correlation is seen when including a range of galactic environments, e.g. of HI clouds in the Milky Way ([Gerrard et al. 2024](#)) and SMC ([Gerrard et al. 2023](#)) in addition to those of molecular clouds in the Milky Way and LMC (e.g. [Padoan et al. 1997](#); [Brunt 2010](#); [Ginsburg et al. 2013](#); [Federrath et al. 2016b](#); [Menon et al. 2021](#); [Marchal & Miville-Deschênes 2021](#); [Sharda & Krumholz 2022](#)), although this is still limited to small number statistics. Additionally, many of studies assessing the properties of gas density PDFs use different methodologies and observational tracers (cf. [Schneider et al. 2022](#), and references therein), as well as different atomic or molecular transitions to assess the kinematics of gas. Although there is still clearly much to understand about these relationships, there is strong theoretical support of a connection between gas density variance and mach number, and emerging observational support for this relationship from observations. Furthermore, there is numerical evidence that the CO molecular linewidth tracks the turbulent velocity dispersion (e.g. [Szűcs et al. 2016](#)), thus providing support for the use of molecular transitions as probes of the initial velocity field of a molecular cloud.

### Appendix A.2: Estimates of Turbulent Gas Velocity Dispersion

There are multiple possible contributions to velocity dispersion measured from line emission in molecular clouds. We summarize the various contributions as follows:

$$\sigma_{v,\text{obs}}^2 \approx \sigma_{v,\text{inst}}^2 + \sigma_{v,T}^2 + \sigma_{v,NT}^2 + \sigma_{v,ls}^2 \quad (\text{A.1})$$

where  $\sigma_{v,\text{obs}}$  is the total measured dispersion,  $\sigma_{v,T} = c_s$  is the thermal contribution to the velocity dispersion,  $\sigma_{v,ls}$  is the background contribution (either from large-scale motions due to shear, streaming, or rotation),  $\sigma_{v,\text{inst}}$  is the instrumental contribution from limited observational velocity resolution, and  $\sigma_{v,NT}$  is the non-thermal contribution.

### Appendix A.2.1: $\sigma_{v,\text{inst}}^2$

The instrumental contribution is easily accounted for, and is subtracted in quadrature from the measured velocity dispersion,  $\sigma_{v,\text{corr}}^2 = \sigma_{v,\text{obs}}^2 - \sigma_{v,\text{inst}}^2$ , where  $\sigma_{v,\text{corr}}$  is the corrected velocity dispersion,  $\sigma_{v,\text{inst}} = \Delta v/2\pi$ , and  $\Delta v$  is the velocity channel

width of the data (cf. [Rosolowsky & Leroy 2006](#)). Velocity dispersion measurements from the previous studies we refer to have been corrected for the instrumental contribution ([Sun et al. 2020](#); [Brunetti et al. 2021, 2024](#)).

### Appendix A.2.2: $\sigma_{v,T}^2$

Typical molecular gas kinetic temperatures of clouds in the Milky Way disk range from  $T_{\text{kin}} \approx 10 - 20$  K (cf. [Heyer & Dame 2015](#)), resulting in thermal sound speeds of  $c_s \approx 0.2 - 0.3$  km s<sup>-1</sup>. Higher kinetic temperatures are estimated for some clouds in the CMZ, possibly due to the enhanced turbulent heating (e.g.  $T_{\text{kin}} \approx 55 - 125$  K from H<sub>2</sub>CO, [Ao et al. 2013](#)), giving rise to higher sound speeds of  $c_s \approx 0.4 - 0.7$  km s<sup>-1</sup>. Additionally, [Friesen et al. \(2017\)](#) find that gas kinetic temperature derived from ammonia (NH<sub>3</sub>) increases with star formation activity in Milky Way clouds. Thus, molecular gas temperature in clouds depends on both galaxy environment and star formation evolutionary stage.

Typical temperatures of clouds in mergers can range from those typical of disk galaxies (e.g.  $T_{\text{kin}} \approx 10 - 20$  K in Arp 55, an intermediate stage merger) to temperatures similar to those in the CMZ (e.g.  $T_{\text{kin}} \approx 110$  K in NGC 2623, a merger remnant, [Sliwa et al. 2017](#)). We can therefore also expect a range of average molecular gas kinetic temperatures across galaxy types. In our models, we our estimates of  $\langle T_{\text{kin}} \rangle$  (described in section 2.3) range from  $\langle T_{\text{kin}} \rangle = 10$  K to  $\langle T_{\text{kin}} \rangle = 65$  K, and find sound speeds ranging from a typical  $c_s \approx 0.2$  km/s in the PHANGS-type galaxy cloud models to  $c_s \approx 0.3$  km/s and  $c_s \approx 0.4$  km/s in the Antennae- and NGC3256-type galaxy cloud models. We note that thermal contributions are not subtracted from the velocity dispersion measurements we use ([Sun et al. 2020](#); [Brunetti et al. 2021, 2024](#)), but this contribution will be small relative to the non-thermal contributions as we discuss below.

### Appendix A.2.3: $\sigma_{v,NT}^2$

The relative thermal and non-thermal contributions to velocity dispersion are still uncertain in molecular clouds. Constraints on the ratio between  $\sigma_{v,T}^2$  and  $\sigma_{v,NT}^2$  in the literature arise largely from Milky Way studies of ammonia, NH<sub>3</sub>, (e.g. [Myers et al. 1991](#); [Pineda et al. 2010](#); [Chen et al. 2019](#); [Choudhury et al. 2021](#); [Friesen & Jarvis 2024](#)), a known tracer of molecular gas kinetic temperature ([Ho & Townes 1983](#)), with some studies including other molecular line transitions (e.g. C<sub>3</sub>H<sub>2</sub> [Myers et al. 1991](#), CCS [Foster et al. 2009](#), N<sub>2</sub>H<sup>+</sup> [Sokolov et al. 2019](#); [Yue et al. 2021](#)). These molecular lines are primarily sensitive to gas denser than  $n > 10^3$  cm<sup>-3</sup>. Thus, these Milky Way studies tend to focus on dense clumps and cores on  $\sim$ sub-parsec scales, as opposed to the bulk of molecular gas in clouds ( $n \gtrsim 10$  cm<sup>-3</sup>) existing on tens of parsecs. In a study of cores in Perseus ( $\sim 0.1$  pc) in ammonia and CCS, [Foster et al. \(2009\)](#) find that a typical ratio of non-thermal to thermal linewidths of  $\sim 0.6$  in protostellar and starless cores, with a range from  $\sim 0.2$  to  $\sim 1$ . In a study of ammonia and N<sub>2</sub>H<sup>+</sup> in the Orion Molecular Cloud 2 and 3, [Yue et al. \(2021\)](#) find that there is a transition from supersonic to transonic turbulence at  $\sim 0.05$  pc, and a transition from transonic to subsonic turbulence between  $\sim 0.05$  pc and  $\sim 0.006$  pc. Thus, at small scales we expect the thermal linewidth to be comparable to the non-thermal linewidth. In this work, we are primarily concerned with the largest scales relevant to molecular clouds.

Power law relationships between the size, measured velocity dispersion, and gas surface density (i.e. Larson's relations) of

whole molecular clouds are well-established in the Milky Way and nearby galaxies (cf. Larson 1981; Heyer & Dame 2015; Miville-Deschênes et al. 2017; Rosolowsky et al. 2021; Schinnerer & Leroy 2024). Studies of the velocity field *within* clouds also find a power law scaling, with larger, supersonic velocity dispersions associated with larger ( $\gtrsim$  parsec) scales (e.g. Choudhury et al. 2021; Yue et al. 2021). At the largest scales of molecular clouds (corresponding to densities  $n \sim 10 \text{ cm}^{-3}$ ), gas temperature only weakly varies with gas density (cf. Glover & Mac Low 2007a,b), suggesting that molecular gas temperatures will not change significantly at the scales associated with larger velocity dispersions measured by, e.g. CO. Thus, at small scales we expect the thermal contribution to the velocity dispersion to be comparable to non-thermal component, and for the relative contribution of the non-thermal component to increase towards larger scales in the turbulent envelopes of clouds. We note that the interpretation of the nature of large linewidths are still debated (Ballesteros-Paredes et al. 2011), but it is clear that the nonthermal component of molecular linewidth increases towards larger scales in clouds.

#### Appendix A.2.4: $\sigma_{v,l,s}^2$

We also consider how large-scale motions of gas, such as galactic shear or cloud rotation, might contribute to velocity dispersion measurements from CO. The impact of shear on a molecular cloud in a normal disk galaxy can be estimated using the Oort Constant  $A$  (Fleck & Clark 1981; Utomo et al. 2015), and depends on the radius at which the molecular cloud resides ( $R_0$ ), as well as the rotational speed of the galaxy at that radius ( $V_0$ ):

$$\Omega_{\text{shear}} = \left| \frac{\Delta v}{\Delta r} \right| = |2A| = \left| \frac{V_0}{R_0} - \left( \frac{dV}{dR} \right)_0 \right| \quad (\text{A.2})$$

where  $V(R)$  is the rotation curve of the galaxy. Clouds that experience the most significant shear in a disk galaxy are therefore those closest to the galaxy center. We use the analytical fits to the rotation curves of the PHANGS galaxies from Lang et al. (2020) to estimate shear as a function of galaxy radius. We assume the internal rotational velocity of a cloud is equivalent to the shear it experiences from Eq. A.2 ( $\Omega = \Omega_{\text{shear}}$ ), and estimate the ratio of cloud rotational energy to turbulent energy in the PHANGS galaxies using (Goodman et al. 1993; Utomo et al. 2015):

$$\gamma_{\text{rot}} = \frac{p\Omega^2 R^2}{3\sigma_v^2} \quad (\text{A.3})$$

where  $R = 45 \text{ pc}$  and  $p = 2/5$  for a uniform sphere. Using this estimation, we find less than 0.02% of the clouds measured in the PHANGS sample (also with analytical velocity curves from Lang et al. 2020) have  $\gamma_{\text{rot}} > 1$ . Therefore, velocity dispersion measurements of the PHANGS galaxies are turbulent velocity motions. We also note that PHANGS galaxies are selected to have low inclination, which reduces blending of molecular line emission along our line of sight and thus optimizes estimates of cloud properties such as turbulent velocity dispersion.

Shear estimates are more difficult to obtain in more disturbed galaxies, such as mergers, as gas motions are non-circular and potentially driven more by streaming motions (e.g. Bournaud et al. 2008; Barnes & Hernquist 1996). Brunetti & Wilson (2022) assess whether clouds around the northern nucleus of NGC 3256 show evidence of alignment, which may be an indication of cloud shear. However, they find no clear evidence of cloud alignment. Thus, it is possible that shear does not play a significant role in the dynamics of molecular clouds in this merger.

An analysis of this kind has not been performed on clouds in NGC4038/9.

For comparison, gas within the bars of barred galaxies do experience more shear and shocks as a result of streaming motions (e.g. Kim et al. 2024), but will also have lower associated  $b$  values. For example, simulations predict  $b \approx 0.22$  for clouds in the CMZ, which also appear to have higher total and turbulent velocity dispersions relative to the disk (Federrath et al. 2016a). As we mention in section 2.2, due to the overall uncertainty in  $b$  we assume  $b = 0.4$  which represents stochastic mixing of turbulent modes (divergence-free and curl-free, or solenoidal and compressive, respectively). Ultimately, contributions to  $\sigma_v$  from large scale motions as well as the uncertainty in  $b$  may impact our estimates of the variance of the  $n$ -PDF (Eq. 3). It is therefore possible that this will contribute some scatter to the intensities and emissivities of our models, but ultimately these uncertainties will not change the overall trends we explore in this paper.

## Appendix B: Variations in Molecular Abundance

We consider the impact of varying HCN and CO abundance on our model results, and we run four additional sets of models using  $x_{\text{HCN}} = 10^{-9}$ ,  $x_{\text{HCN}} = 10^{-7}$ ,  $x_{\text{CO}} = 1.4 \times 10^{-3}$ , and  $x_{\text{CO}} = 1.4 \times 10^{-5}$ . We note that  $x_{\text{CO}} = 1.4 \times 10^{-3}$  is higher than we expect to find in real molecular clouds (cf. Bolatto et al. 2013), but we use this value to consider a wide range of CO abundances. We find that increasing (decreasing) HCN and CO abundance has the effect of increasing (decreasing) the optical depths of the molecular gas tracers, which is a product of molecular column density scaling with molecular abundance in our models. We find mean CO optical depths of  $\tau_{\text{CO}} \approx 2.7$ , 16.9, and 107.2 for  $x_{\text{CO}} = 1.4 \times 10^{-5}$ ,  $1.4 \times 10^{-4}$ , and  $1.4 \times 10^{-3}$ , respectively. Mean HCN optical depths are found to be  $\tau_{\text{HCN}} \approx 0.88$ , 6.1, and 36.5 for  $x_{\text{HCN}} = 10^{-9}$ ,  $10^{-8}$ , and  $10^{-7}$ , respectively. The impact of varying abundance on CO optical depth is therefore more significant relative to HCN and is a result of bright CO emission spanning a broader range of column densities relative to HCN in our models (see Fig. 1). Optical depths are plotted against molecular intensities for each of these abundances in Fig. B.1.

We also find that increasing (decreasing) molecular abundance slightly increases (decreases) the median intensity (and, similarly, emissivity, see Eq. 1) in our models. We find  $I_{\text{CO}} \approx 63.0$ , 47.9, and 37.1  $\text{K km s}^{-1}$  for  $x_{\text{CO}} = 1.4 \times 10^{-3}$ ,  $1.4 \times 10^{-4}$ , and  $1.4 \times 10^{-5}$ , respectively. HCN intensity appears to vary in roughly regular steps with molecular abundance (see Fig. B.1), with  $I_{\text{HCN}} \approx 8.9$ , 2.2, and 0.7  $\text{K km s}^{-1}$  for  $x_{\text{HCN}} = 10^{-7}$ ,  $10^{-8}$ , and  $10^{-9}$ , respectively. Furthermore,  $x_{\text{HCN}} = 10^{-9}$  appears to produce HCN intensities that are also consistent with measurements from our sample (cf. Paper I) (relative to  $x_{\text{HCN}} = 10^{-8}$ ), and some of the higher  $I_{\text{HCN}}$  measurements of the EMPIRE sample (Jiménez-Donaire et al. 2019). As shown in Fig. B.1, there is a subsample of measurements with higher  $I_{\text{CO}}$  that have HCN/CO ratios that fall below those produced by our models assuming  $x_{\text{HCN}} = 10^{-8}$ . It may be possible that these sources (which are mostly comprised of the more extreme systems in our sample) have a lower HCN abundance, on average. A higher HCN abundance ( $x_{\text{HCN}} = 10^{-7}$ ) is likely not realistic for most molecular clouds (cf. Viti 2017), and also appears to produce higher HCN/CO ratios than what is measured in our sample and the EMPIRE sample.

In summary, the optical depth for  $x_{\text{CO}} = 1.4 \times 10^{-3}$  is  $\sim 6$  times larger than that for  $x_{\text{CO}} = 1.4 \times 10^{-4}$ , but this makes little difference to the main conclusions of this paper as  $\tau_{\text{CO}} > 10$  and CO is in LTE for both of these values for the majority of

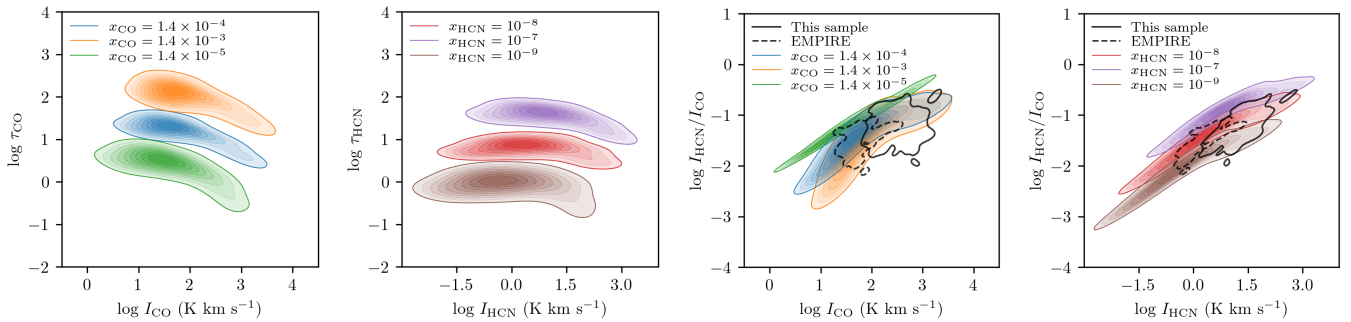


**Fig. B.1.** *Left:* Modelled CO optical depth as a function of CO intensity for  $x_{\text{CO}} = 1.4 \times 10^{-5}$  (green contours)  $x_{\text{CO}} = 1.4 \times 10^{-4}$  (blue contours)  $x_{\text{CO}} = 1.4 \times 10^{-3}$  (orange contours). *Left center:* Modelled HCN optical depth as a function of HCN intensity for  $x_{\text{HCN}} = 10^{-9}$  (brown contours),  $x_{\text{HCN}} = 10^{-8}$  (red contours), and  $x_{\text{HCN}} = 10^{-7}$  (purple contours). *Right center:* The modelled HCN/CO intensity ratio as a function of CO optical depth for varying CO abundance. The HCN intensities are for  $x_{\text{HCN}} = 10^{-8}$ . *Right:* The modelled HCN/CO intensity ratio as a function of CO optical depth for varying HCN abundance. The CO intensities are for  $x_{\text{CO}} = 1.4 \times 10^{-4}$ . Ten contours are drawn in even steps from the 16<sup>th</sup> to 100<sup>th</sup> percentile. Contours are shown in the right two panels for our sample of galaxies and the EMPIRE sample as the solid black and dashed black contours, respectively.

our models, resulting in similar intensities and emissivities, and likewise similar results. For  $x_{\text{CO}} = 1.4 \times 10^{-5}$ , the modelled CO ranges from only moderately optically thick to optically-thin ( $\log \tau < 0$ ). Since CO emission is likely optically thick in most molecular clouds, these results are not considered for analysis. We therefore focus on the results using the Solar CO abundance,  $x_{\text{CO}} = 1.4 \times 10^{-4}$ , in the main text. We find that both  $x_{\text{HCN}} = 10^{-8}$  and  $x_{\text{HCN}} = 10^{-9}$  produce HCN intensities and HCN/CO ratios consistent with measurements in our sample and the EMPIRE sample. It is possible that the actual HCN abundances in the galaxies considered here vary between  $x_{\text{HCN}} = 10^{-8}$  and  $x_{\text{HCN}} = 10^{-9}$  (cf. Viti 2017). It is also possible that more extreme systems trend towards lower HCN abundance, but this is highly uncertain due to a lack of data of optically-thin dense gas tracers. We therefore focus on the results of  $x_{\text{HCN}} = 10^{-8}$  in the main text and note that many of main conclusions would remain similar using a different value of  $x_{\text{HCN}}$ , with slight offsets in HCN intensity and emissivity.

### Appendix C: The Impact of Sensitivity Limits

We re-derive emissivity from our models by excluding the low-density regions of our models that have HCN intensities below  $\sim 0.1 \text{ K km s}^{-1}$  (roughly the sensitivity limit in Tafalla et al. 2023) and show our results in Fig. C.1. We find that this has the effect of shifting  $\alpha_{\text{HCN}}$  to smaller values and more strongly impacts  $\alpha_{\text{HCN}}$  from the PHANGS-type models. This is because much of the emission in our PHANGS-type models resides at lower gas column densities. Additionally, the  $\alpha_{\text{HCN}}$  derived by Tafalla et al. (2023) appear more consistent with models in our sample that have larger gas surface density and larger velocity dispersion (i.e. the models based on measurements from the Antennae and NGC3256 mergers). From Fig. 3. in Tafalla et al. (2023), we can see that the emission from their dense gas tracers appears to extend below their sensitivity limit, suggesting they are indeed missing some emission at low HCN intensity and low column density. Thus, this discrepancy could be because our models include emission from HCN arising from lower column densities below the detection limit of their study. As we find, this will disproportionately affect clouds with more emission at lower gas surface densities.



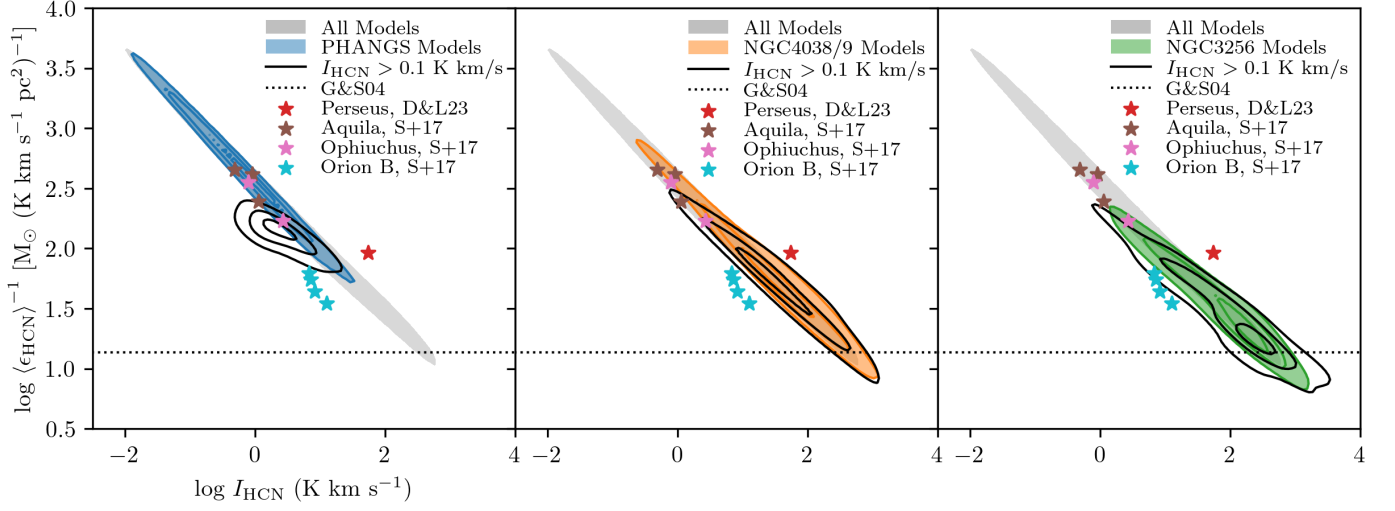


**Fig. C.1.** The inverse of the HCN emissivity (in units of the HCN conversion factor) as a function of HCN intensity. We plot the PHANGS-, NGC4038/9-, and NGC3256-type models from left to right as the blue, orange, and green filled contours. The black contours represent  $\langle \epsilon_{\text{HCN}} \rangle^{-1}$  for the models where we make a cut at  $0.1 \text{ K km s}^{-1}$ , which is analogous to a sensitivity limit in observations. For comparison, we also show the Gao & Solomon (2004a,b) value as the black, dotted horizontal line and several published values of  $\alpha_{\text{HCN}}$  from observations of Milky Way clouds (Dame & Lada 2023; Shimajiri et al. 2017). The gray, filled contour represents all models. We find the HCN emissivities from the PHANGS-type models to be most strongly impacted by a sensitivity cut. These models appear to have artificially lower  $\langle \epsilon_{\text{HCN}} \rangle^{-1}$  (higher emissivity) as a result of the cut.